Hubble Space Telescope Ultraviolet Images of Five Circumnuclear Star-Forming Rings [1]

Dan Maoz

School of Physics & Astronomy and Wise Observatory, Tel-Aviv University,
Tel-Aviv 69978, Israel, dani@wise.tau.ac.il

Aaron J. Barth

Department of Astronomy, University of California, Berkeley, CA 94720-3411

Amiel Sternberg

School of Physics & Astronomy, Tel-Aviv University, Tel-Aviv 69978, Israel

Alexei V. Filippenko

Department of Astronomy, University of California, Berkeley, CA 94720-3411

Luis C. Ho

Department of Astronomy, University of California, Berkeley, CA 94720-3411,
and Center for Astrophysics, 60 Garden Street, Cambridge, MA 02138

F. Duccio Macchetto

Space Telescope Science Institute, 3700 San Martin Dr., Baltimore, MD 21218

Hans-Walter Rix

Max-Planck-Institut für Astrophysik, Karl-Schwarzschild-Strasse 1, D-85740 Garching,
Germany, and Steward Observatory, University of Arizona, Tucson, AZ 85721

and Donald P. Schneider

Department of Astronomy and Astrophysics, The Pennsylvania State University,
University Park, PA 16802

ABSTRACT

We present UV (~ 2300 Å) images, obtained with the *Hubble Space Telescope* (*HST*) Faint Object Camera, of the central $20''$ of five galaxies containing circumnuclear star-forming rings. The five galaxies are from a well-defined

---

[1]Based on observations with the *Hubble Space Telescope*, which is operated by AURA, Inc. under NASA contract NAS 5-26555

sample of 103 normal, nearby galaxies we have observed with *HST*. At the *HST* resolution (0.05″), the rings break up into discrete star-forming clumps. Each clump is composed of many luminous ($L_\lambda(2300\text{Å}) \approx 10^{35} - 10^{37}$ erg s^{-1} Å^{-1}) and compact ($R \lesssim 5$ pc) star clusters. These objects are similar to those that have been recently reported in colliding and starburst galaxies, and in several other circumnuclear rings. A large fraction, 15%–50%, of the UV emission originates in these compact clusters. Compact clusters therefore may be the preferred mode of star formation in starburst environments.

For one galaxy, NGC 2997, we measure the UV-optical colors of the individual clusters using an archival *HST* WFPC2 image at ~ 6000 Å. Comparing the colors and luminosities to starburst population synthesis models, we show that the clusters are less than 100 Myr old and have masses of at least a few $10^3 M_\odot$, with some as high as $10^5 M_\odot$. The UV extinction to those clusters that are detected in the UV is at most a factor of 10. In NGC 2997, the limits on the masses and the ages of the young clusters indicate that these objects will remain bound and evolve into globular clusters. However, data in additional wavebands are needed to critically test this hypothesis.

The luminosity function of the clusters in the rings is similar in shape to those measured for super star clusters in other star-forming galaxies, and extends to luminosities lower by several orders of magnitude. All five of the UV-detected circumnuclear rings occur in barred or weakly barred spiral galaxies of type Sc or earlier. None of the five rings has an active nucleus at its center, arguing against a direct correspondence between circumnuclear star formation and nuclear activity.

Subject headings: galaxies: star clusters – galaxies: starburst – galaxies: nuclei

To Appear in the Astronomical Journal, June 1996

1. Introduction

One of the most intriguing results of galaxy imaging with the high angular resolution of the *Hubble Space Telecope (HST)* has been the discovery of extremely luminous, compact, young star clusters in a variety of starburst environments. These include the cooling-flow/merger-remnant galaxy NGC 1275 (Holtzman et al. 1992), merging galaxies (Whitmore et al. 1993; Conti & Vacca 1994; Whitmore & Schweizer 1995), "amorphous" peculiar galaxies (Hunter, O'Connell, & Gallagher 1994; O'Connell, Gallagher, & Hunter

1994; O'Connell et al. 1995), two barred galaxies with circumnuclear rings (Barth et al. 1995), and nine starburst galaxies with a range of morphologies and luminosities (Meurer et al. 1995). Prior to *HST*, only a few objects of this type were known to exist (e.g., Arp & Sandage 1985; Melnick, Moles, & Terlevich 1985); the severe crowding in most starbursts prevents their resolution into individual clusters in ground-based images. Similar objects have been detected recently in high-resolution infrared images of the starburst galaxy NGC 1808 (Tacconi-Garman, Sternberg, & Eckart 1996).

Such "super star clusters," having diameters not exceeding a few tens of parsecs and luminosities greater than $M_V = -10$ mag, result from extreme episodes of rapid star formation which are virtually absent in ordinary galactic disks. The small radii, high luminosities, and presumably high masses of these clusters have led to suggestions that, as opposed to standard OB associations, they may remain bound systems. If so, after 10^{10} years they would have magnitudes comparable to those of old Galactic globular clusters, and therefore could be present-day versions of young globular clusters. Van den Bergh (1995) has argued that the sizes and luminosity functions of the young clusters more closely resemble those of Galactic open clusters than those of globular clusters. Meurer (1995b) counters that the sizes of the young clusters are often poorly constrained in the *HST* data, and that the luminosity functions of the globular clusters and the super star clusters should not be directly compared because the super star clusters in a given galaxy are not all necessarily of the same age and so are viewed at different epochs (and luminosities) in the clusters' evolution. Note that luminous, compact clusters are also known in our Galaxy and the Large Magellanic Cloud (LMC). For example, recent *HST* and near-infrared observations of the R136 cluster in 30 Doradus in the LMC indicate a mass of $\sim 10^4 M_\odot$ within a radius of 2.5 pc (Brandl et al. 1996). The dynamical crossing time for such a cluster is 3×10^5 yr, while the measurements constrain the stellar ages to 3–5 Myr. This system is therefore bound, and could also evolve into a low-mass globular cluster. The limits on luminosity used to define super star clusters and distinguish them from the more common and slightly less-luminous compact clusters are arbitrary; physically, these are all similar objects. Clearly, learning more about these young clusters can shed light on rapid star formation, globular-cluster formation, and the possible connections between them.

The bulges of some nearby spiral galaxies display intense star formation in a ring of optical "hot-spots" (Sérsic & Pastoriza 1967). Such galaxies offer us an opportunity to study starburst properties at a level of detail that would be impossible for more distant or more heavily obscured systems. Kiloparsec-sized nuclear rings can form as a result of bar-driven inflow to an inner Lindblad resonance (e.g., Tubbs 1982; Athanassoula 1992; Piner et al. 1995), yielding a large concentration of dense gas in a small region surrounding the nucleus (Kenney et al. 1992). Several nuclear rings have been studied extensively from

the ground (e.g., Hummel, van der Hulst, & Keel 1987), but the small sizes of the rings (typically $\sim 10''$) have precluded detailed studies of their structure. *HST* imaging has opened a new vista on these hot-spot galaxies. WFPC, WFPC2, and FOC images have revealed large populations of super star clusters in nuclear rings in four nearby galaxies: NGC 4314 (Benedict et al. 1993), NGC 1097 and NGC 6951 (Barth et al. 1995), and NGC 3310 (Meurer et al. 1995).

The process of cluster formation in these starbursts appears to be physically distinct from normal star formation in spiral galaxies. Even the most luminous disk H II regions in late-type galaxies seldom contain compact clusters that might be potential young globulars (Kennicutt & Chu 1988). The occurrence of super star clusters may be unique to starburst environments. Hot-spot H II regions are also spectroscopically distinct from disk H II regions; the hot-spot H II regions have higher heavy-element abundances and possess lower emission-line equivalent widths than disk H II regions of the same luminosity, suggesting that continuous, intense star formation occurs within the hot-spots (Kennicutt, Keel, & Blaha 1989; Mayya 1995). Circumnuclear hot-spots contain over 50% of the massive star formation in some galaxies (Phillips 1993); thus, determining the physical parameters of hot-spot H II regions is important for understanding the global star formation properties of spirals.

We have carried out a UV imaging survey with the *HST* Faint Object Camera (FOC) of the central regions of 103 large, nearby galaxies, selected randomly from a complete sample of 240 galaxies. An atlas of the survey is presented by Maoz et al. (1996), where full details of the sample selection, observations, and data reduction are given. One of the main purposes of the survey is to study star formation in the central regions of the galaxies. By observing at ~ 2300 Å, the survey images detect predominantly the youngest existing stellar populations and thus provide a clean probe of the most recent sites of active star formation, uncontaminated by light from more evolved stars.

In this paper, we present results for five out of the 103 galaxies, whose UV images display circumnuclear star-forming rings. In a forthcoming paper (Ho et al. 1996c) we will analyze star formation based on the UV images of the other sample galaxies. In §2, below, we describe the observations and data analysis. Notes on the individual galaxies are given in §3. We discuss the physical implications of the data in §4 and summarize our results in §5.

2.   Observations and Analysis

The five galaxies described in this paper were observed with *HST* in 1993, June and July. Here we briefly outline the sample from which the five galaxies are taken, the observations, and the data reduction. More complete details are given in Maoz et al. (1996).

The sample consists of all galaxies in the UGC and ESO catalogs (Lauberts & Valentijn 1989) with heliocentric velocities less than 2000 km s^{-1} and photographic diameters (as defined in the catalogs) greater than 6$'$. Exclusion of 22 galaxies for a number of reasons (see Maoz et al. 1996) left 240 galaxies from which the Space Telescope Science Institute (STScI) staff chose Snapshot targets based only on scheduling convenience. A total of 103 out of the 240 sample galaxies were successfully observed while the program was active.

Data were obtained with the *HST f/*96 Faint Object Camera (FOC; Paresce 1990) in its "zoomed" 1024×512-pixel mode with $0.022'' \times 0.044''$ pixels, giving a field of view of $22'' \times 22''$. The F220W filter was used. This is a broad-band filter with an effective wavelength of ~ 2300 Å and effective bandpass of ~ 500 Å. The exposure time was 10 minutes per galaxy. The images were processed by STScI's "pipeline" reduction (Baxter et al. 1994), after which the pixel scale is $0.0225''$ pixel^{-1}. All our data were obtained before the *HST* repair mission at the end of 1993, and therefore are affected by spherical aberration. As a result, the point-spread function (PSF) consists of a sharp core of full width at half maximum (FWHM) $\sim 0.05''$ that contains about 15% of the light, with the rest of the light spread in a complex low-level "halo" with a radius of several arcseconds (Burrows et al. 1991). In the observing mode we have used, the FOC is limited in its dynamic range to 255 counts (8 bits) per zoomed pixel; additional signal causes the counts to "fold over" and start again from 0. Another problem is that the detected count rate becomes nonlinear, gradually saturating for bright sources (see Baxter et al. 1994). The central pixels of most of the compact bright sources detected in the images may be in the nonlinear regime, and the brightest of them are clearly saturated. Our analysis will therefore rely mainly on the wings of the PSF, which have low count rates ($\lesssim 0.05$ s^{-1} pixel^{-1}). We model the PSF using a well-exposed F220W image of a star observed with the FOC $f/$96 256×256 pixel mode, which has a large dynamic and linear range (but small field of view). Such empirical PSFs are required for work in the UV (Baxter et al. 1994).

As in Maoz et al. (1995, 1996), we translate the FOC counts to a flux density f_λ at 2270 Å assuming 1 count s^{-1} = 1.66×10^{-17} erg s^{-1} cm^{-2} Å^{-1}, based on the on-line calibration data available from STScI for the FOC and F220W filter, with a 25% increase in sensitivity of the 512×1024 zoomed-pixel mode relative to the 512×512 pixel mode (Baxter et al. 1994). This calibration assumes a spectrum that is constant in f_λ. As detailed in Maoz et al. (1995), the F220W count-rate vs. f_λ at 2270 Å is weakly dependent

on the spectral slope, with a change of only a few percent for a large range in slopes.

The uncertainty in the absolute flux is $\sim 20\%$ when measuring individual compact sources (Baxter et al. 1994), but can be as small as $\sim 5\%$ when measuring the UV flux integrated over large areas (e.g. ~ 150 arcsec^2; Meurer 1995a), if the background can be reliably determined.

In the analysis below, we also use a pair of optical images of NGC 2997 taken on 1994 June 21 (after the repair mission) with the *HST* WFPC2, and obtained from the *HST* archive. They are two 80 s exposures through the F606W filter (similar to V-band). The star-forming ring of interest is on the PC detector, which has a pixel scale of $0.045''$ pixel^{-1}. The images were pipeline processed, registered, and co-added to reject cosmic-ray hits. Counts were converted to flux at 6060 Å using the STScI pipeline calibration and assuming a flat spectrum in f_λ.

The FOC images show a variety of morphologies and UV brightnesses in the centers of the galaxies (Maoz et al. 1996). Maoz et al. (1995) analyzed the data for nine galaxies whose images show conspicuous bright and compact sources at the galaxy nucleus. In this paper, we present results for five out of the 103 galaxies, whose UV images display circumnuclear star-forming rings. The five were found by visually examining all the images for any UV-emission morphology roughly surrounding the nucleus (i.e., the center of the image) in a ring, or in patches roughly forming a ring. Four of the five galaxies selected in this way are already known from previous ground-based images to be galaxies with circumnuclear star-forming rings (NGC 1433, NGC 1512, NGC 2997, NGC 5248; see §3). One of the five, NGC 1079, was not previously known to be a circumnuclear-ring galaxy, probably due to its small ($4''$) ring diameter. As we show below, the physical size and properties of its ring are similar to those of the other four galaxies. Figure 1 displays the FOC UV images of four of the rings. Figure 2 shows the FOC (UV) and WFPC2 (optical) images of NGC 2997, shown with matched orientation and scale. Table 1 lists the main characteristics of the ring galaxies.

As seen in Figures 1 and 2, the rings in the *HST* images break up into a number of clumps, with each clump consisting of many compact sources on top of a diffuse background. The background is highly irregular and often cut by dust lanes. (The detail afforded by the *HST* angular resolution can be appreciated by comparing NGC 1512 in Fig. 1 to a ground-based Hα image in Fig. 2 of Kennicutt [1994].) Note that not only is the area exterior to the rings mostly devoid of UV emission, but so is the region interior to the rings, including the nuclei of the galaxies. We have matched up the gross features of the rings with optical ground-based images (and in the case of NGC 2997, with an optical *HST* image; see §3.4 and Fig. 2), and verified that the nucleus of the galaxy is indeed within the ring but

invisible in the UV (except for NGC 1512, which has a faint nuclear UV source). This shows that, despite the high nuclear surface brightnesses, little visual-band light leaks through the F220W filter (see also Maoz et al. 1996), and mostly the youngest stellar populations are registered in the images. (The "UV-upturn" observed in some elliptical galaxies and some spiral-galaxy bulges [e.g., Burstein et al. 1988], and thought to originate from evolved stars, sets in at $\lambda \lesssim 2000$ Å, and may contribute some of the diffuse UV emission we observe.) We list in Table 1 the total 2270 Å flux from each of the rings. We measured it by summing the counts above the background, which was determined in the empty corners of each image. The main background source at ~ 2300 Å is particle induced, and variable throughout the *HST* orbit (Nota, Jedrzejewski, & Hack 1995). Since the galaxies observed are much larger than the field of view, we cannot exclude some contribution to the background from diffuse UV emission from the galaxies themselves. The UV fluxes quoted in this paper are uncorrected for Galactic or intrinsic extinction. Galactic extinction is negligible for the galaxies discussed here, except for NGC 2997, which has $E(B-V) = 0.1$ mag (Burstein & Heiles 1982; see also §4.2), corresponding to a UV extinction $A_{2300} \approx 0.8$ mag.

The compact sources distributed along the rings are reminiscent of the super star clusters detected in optical and UV *HST* images of other starburst galaxies (see §1). To study their properties, we have measured the brightnesses and intrinsic sizes of the individual sources. At least some of the diffuse emission surrounding the bright compact sources is an artifact of the spherically-aberrated PSF. By summing the contribution of the individual sources to the total UV light, we can estimate what fraction of the active star formation in the rings is occuring within these compact objects.

To identify all compact sources in each image in a fairly objective way, the DAOFIND algorithm in the IRAF [2] implementation of DAOPHOT (Stetson 1987) was applied to the data. The threshold for detection of a source above the background was set low enough so that most of the objects clearly discerned by visual inspection would be detected, but high enough to avoid an excessively large number of false identifications of artifacts and noise peaks. A fair number of sources was always missed by DAOFIND, due to the complicated background, and a number of false identifications made, e.g., at the intersection of PSF rings. The detected objects were therefore marked on a screen, obvious misidentifications were deleted, and obvious sources that were missed by the algorithm were added to the list of detected sources. Although this process is not completely objective, it is the best compromise we have found for these data.

---

[2]IRAF (Image Reduction and Analysis Facility) is distributed by the National Optical Astronomy Observatories, which are operated by Aura, Inc., under cooperative agreement with the National Science Foundation.

As already noted, the central pixels of every compact source are suspect of nonlinearity and/or saturation, and so cannot be used in a conventional PSF-fitting-based crowded-field photometry program. Maoz et al. (1995) fitted empirical PSFs to the azimuthally-averaged radial profiles of bright nuclear sources from this survey, between radii of $0.4''$ and $2.2''$ (i.e. the "rings" and "halo" of the PSF), excluding the central, saturated pixels. The sources detected in the ring galaxies discussed here are significantly fainter than those nuclear sources and are also crowded, so this technique is not applicable. Instead, we follow Meurer et al. (1995) and fit the sources with the radial profile calculated in the wings of an empirical PSF, at radii of $0.044''$ to $0.2''$ (i.e., 2 to 10 pixels, again excluding the central, high count-rate pixels). For the brightest compact sources in the rings, where the PSF wings are also saturated, we use the Maoz et al. (1995) algorithm. In either case, the PSF is convolved with Gaussians of varying widths, and its radial profile is scaled in brightness and is added to a constant background so as to minimize the χ^2 fit to the radial profile of each source. The convolved Gaussian width of the best-fit PSF provides an estimate of the intrinsic size of the sources.

To gauge the realiability of the size and brightness measurements in the presence of noise, crowding, and variable background, we have carried out the following experiments. First, we added to the images simulated sources of known brightness and size on regions with different backgrounds, added the appropriate Poisson noise, and then measured the sources. Second (as in Meurer et al. 1995), we tested the algorithm by applying it to the stars in F220W FOC images of the Galactic cluster NGC 104. From these two tests we conclude that compact-source brightnesses can be measured to $\sim 20\%$ accuracy for sources with > 1 count pixel^{-1} at the 2-pixel radius in their radial profiles. Such a brightness corresponds to 250 total reconstructed counts in the source, or 7×10^{-18} erg s^{-1} cm^{-2} Å^{-1} in these 600 s exposures. We have tabulated in this paper only sources whose total reconstructed counts are greater than 100, i.e. $f_\lambda(2270\text{Å}) > 3 \times 10^{-18}$ erg s^{-1} cm^{-2} Å^{-1}. This can be considered the detection limit of these images for relatively isolated sources on a low background. The detection limit is higher in crowded, high surface-brightness regions. Recovering the width of the Gaussian that was convolved with the PSF is more difficult, and is reliable to any degree only for sources with brightness > 4 counts pixel^{-1} at the 2-pixel radius (i.e. $\gtrsim 3 \times 10^{-17}$ erg s^{-1} cm^{-2} Å^{-1}). The resolution limit of the technique is reached for a Gaussian σ of 1.5 pixels (or $0.033''$, i.e. objects with an intrinsic Gaussian FWHM of $< 0.08''$ appear unresolved). Recovered widths are accurate to about 0.5 pixels. Sources wider than 4 pixels are often elongated and faint, and are probably composed of several poorly resolved clusters. Their width is also poorly reconstructed by the technique, which assumes radial symmetry. The width estimate can be led completely astray by crowding or a high and variable background (due to, e.g., the PSF features of another bright source).

All width estimates given below should therefore be treated with caution until confirmed by higher S/N, unaberrated images. The true width is, nevertheless, unlikely to be much larger than in our estimates, since it is difficult to make a source appear more compact than it really is.

The brightnesses of the compact sources in the optical WFPC2 image of NGC 2997 were measured using DAOPHOT aperture photometry, as described in Barth et al. (1995) for the measurement of compact sources in WFPC and WFPC2 optical images of two other circumnuclear ring galaxies, NGC 1097 and NGC 6951. The photometry used a 2-pixel radius aperture, the background was determined in an annulus of radius 4-6 pixels, and an aperture correction was determined using an artificial PSF (created with the Tiny Tim package; Krist 1994), broadened by convolution with a Gaussian to match the mean width of several of the brightest clusters in the image. Due to the inconstant background and the undersampling of the PSF, the typical errors are of order 10%. We tabulate from the optical image objects with $f_\lambda(6060\text{Å}) \geq 1 \times 10^{-18}$ erg s^{-1} cm^{-2} Å^{-1}, which at the distance of NGC 2997 corresponds to $M_V \leq -7$, i.e. brighter than the most luminous individual stars.

Tables 2-6 list the results of the measurements of the individual compact sources for each of the galaxies. The geometrical center was estimated for each ring and is listed in the first line of each table (source No. 0). The offsets of all the sources are listed relative to this coordinate origin. The best-fitting widths are listed only for those sources that are bright and uncrowded enough to make this measurement fairly reliable. For NGC 2997, we have matched those sources appearing in both the UV and optical images, and list them as such in Table 5.

3. Notes on Individual Objects

3.1. NGC 1079

As seen in Figure 1, the ring in this SAB0 galaxy is the smallest in angular extent (4″) which we have detected. This probably explains why it has not been noted before from ground-based observations. At a distance of $16.9h_{75}^{-1}$ Mpc (Tully 1988), the major-axis diameter of the ring is $330h_{75}^{-1}$ pc. To verify that it is, in fact, a star-forming ring (and not, e.g., an edge-brightened "bubble"), we obtained a long-slit spectrum along the ring's major axis. The observations were done on 1993 November 8 UT at the Lick 3-m Shane reflector using the Kast Cassegrain spectrograph (Miller & Stone 1993). Two exposures, each of half hour duration, were obtained with a slit width of 1″, giving a resolution of ~ 2.3 Å over the wavelength range 4550 Å– 5260 Å.

We used stellar and galaxy templates and a least-squares fitting process (Rix & White 1992; Rix et al. 1995) to derive rotation curves along the major axis both for the stars (from stellar absorption features) and for the gas (from emission features). The results (Figure 3) show within $\pm 2''$ (the radius of the ring) the linear rise expected for a ring in projection. Assuming the ring is circular, the axis ratio (~ 2) implies an inclination of $60°$, and a deprojected circular velocity at $2''$-radius of ~ 60 km s^{-1}. The velocity implies a mass interior to the ring of $10^8 M_\odot$, and a mean mass density of $15 M_\odot$ pc^{-3} within the central 160 pc, normal (though somewhat on the low side) for the centers of galaxies. The emission-line spectrum is typical of a starburst.

Similar to the case in some other galaxy bulges (e.g., Fillmore, Boroson, & Dressler 1986; Rix et al. 1995), the measured rotation velocity of the stars is lower than that of the gas. This may have two reasons: First, the stars have a larger degree of support from random motions and hence their streaming motion is smaller. Second, the observed rotation includes an integration along the line-of-sight. If the ionized gas is more centrally concentrated and more flattened than the stars, its rotation will be less affected by this integration.

We identify 19 compact sources in the *HST* UV image, whose brightnesses are listed in Table 2. Comparing their summed contribution (including the PSF halos) to the total UV light measured in the image, we find that 23% of the UV light is contributed by discrete compact sources. In its western half, the ring is either broken or transversed by a dust lane.

3.2. NGC 1433

This SBab galaxy has been noted, apart from its nuclear ring, for several outer rings (Kinney et al. 1993, and references therein). At the angular resolution of the *HST* image, the ring appears irregular and patchy. Interestingly, the nuclear ring in NGC 1512 is much more ordered, even though both galaxies have very similar sizes, luminosities, and morphologies (see Sandage & Bedke 1988, for beautiful pictures of these two galaxies side by side). From comparison of the UV image of NGC 1433 to a ground-based CCD image through a narrow-band Hα filter, we verify that the nucleus of the galaxy is within the UV ring structure, but is dark in the UV.

The major-axis diameter of the ring is $\sim 9.5''$, or $540 h_{75}^{-1}$ pc at a distance of $11.6 h_{75}^{-1}$ Mpc (Tully 1988). We identify 31 compact sources in the image, which contribute 12% of the total UV light.

3.3. NGC 1512

The spiral ring in this SBab galaxy is highly ordered and reminiscent of that seen in NGC 6951 (Barth et al. 1995). The ring major axis is $\sim 15''$, $690h_{75}^{-1}$ pc at a distance of $9.5h_{75}^{-1}$ Mpc (Tully 1988).

We detect 43 compact sources in the image, including one (No. 31) on the southeast side of the ring whose brightness is 1.5 times greater than all the others combined. There is also a faint compact source at or near the nucleus (No. 12). 39% of the UV light is in the detected compact sources, or 16% excluding the brightest source.

3.4. NGC 2997

The nuclear ring of this SABc galaxy has been previously observed from the ground (Meaburn & Terret 1982; Walsh et al. 1986). As in NGC 1433, the ring in the HST UV image is patchy and irregular, and very faint along its southern half. The major-axis diameter is $\sim 8''$, or $540h_{75}^{-1}$ pc at $13.8h_{75}^{-1}$ Mpc. The 39 compact sources we detect contribute 14% of the total UV light.

Fortunately, we have found in the *HST* archive a WFPC2 F606W (i.e. ~ 6060 Å) exposure of this galaxy (see §2). The 155 compact sources we measure in the optical image are listed in Table 5. By computing the coordinate transformation between the UV and optical images, we have been able to identify 24 of the UV-detected sources in the optical image. The UV-optical colors we can extract for individual compact sources in this galaxy provide important information on the physical nature of the sources. We exploit these data further in §4.2. There are 133 optical sources that are undetected in the UV image. The brighter among the optical-only sources may be either aged or highly-reddened star clusters. The fainter of these may also be smeared by the spherical aberration in the UV image into some of the diffuse emission observed there. We examine the potential importance of this effect in §4.1. The faintest among the optical-only sources could also be individual red luminous stars, such as supergiants. The 15 sources (mostly faint) that are detected only in the UV must be either faint young clusters or OB associations, or individual young massive stars. There is no obvious difference in the spatial distributions of the clusters that are detected in either one or both bands.

3.5.   NGC 5248

This SABbc galaxy has a well-ordered nuclear ring. The major-axis diameter is $\sim 11''$, or $1.2h_{75}^{-1}$ kpc at $22.7h_{75}^{-1}$ Mpc. The 46 compact sources we detect contribute 16% of the UV light. The nucleus, which is invisible in the UV, has the optical spectrum of an H II region through a $2'' \times 4''$ aperture at position angle $45°$ (Ho, Filippenko, & Sargent 1995, 1996a). However, this spectrum might have a significant contribution from the H II regions in the ring.

4.   Discussion

4.1.   The Fraction of Light in Compact Sources

The UV luminosities (uncorrected for reddening) of the compact sources distributed in the rings, listed in Tables 2-6, are in the range $L_\lambda(2270\text{Å}) \approx 10^{34.5} - 10^{37.5}$ erg s^{-1} Å^{-1}, where $L_\lambda(2270\text{Å}) \equiv f_\lambda(2270\text{Å})4\pi D^2$ and D is the distance to a galaxy. For reference, $\log L_\lambda(2270\text{Å})$ is 34.4 and 31.2 for a single main-sequence B0 or A0 star, respectively (Allen 1973). The optical luminosities of the objects in NGC 2997, listed in Table 5, are in the range $L_\lambda(6060\text{Å}) \approx 10^{34.3} - 10^{36.2}$ erg s^{-1} Å^{-1}. Also for reference, $M_V = -10$ mag, used by O'Connell et al. (1994) as a defining limit for super star clusters, corresponds to $\log L_\lambda(6060\text{Å}) \approx 35.6$. Those sources bright enough for a size measurement typically have a Gaussian radius of only several pc, and are often unresolved, with upper limits of $\lesssim 2$ pc on their radius. The brighter among these objects are in all respects similar to the "super star clusters" or "young globular clusters" identified in *HST* images of other starburst environments (see §1).[3] It is becoming clear that these compact sources, whatever their nature, are quite common in starburst environments. In the absence of color information, the fainter objects in the UV images could be individual O and B stars. In the optical image of NGC 2297, the faintest sources have luminosities comparable to those of the most luminous red supergiants ($M_V \approx -7$; Allen 1973) and so could also be individual stars.

As shown in §3, a substantial fraction of the UV light, ranging from 10% to 40% among the five rings, is coming from clearly detected sources. Similar fractions were reported in the starburst galaxies analyzed by Meurer et al. (1995). Since the UV images are sensitive

---

[3] Note that the high luminosities of the objects in the galaxy He 2-10, observed with the same observational setup as ours, and reported by Conti & Vacca (1994), result from applying an uncertain extinction correction of a factor of ~ 100 to the UV fluxes. The uncorrected UV luminosities are in the range $\log L_\lambda(2270\text{Å}) \sim 35.5$ to 36.5, similar to that of the compact sources reported here.

mostly to the youngest stellar populations, it appears that these compact clusters are one of the preferred modes of star formation. Furthermore, the fractions given above are lower limits to the true fraction of UV light coming from individual sources, because the overlapping PSF halos of faint objects that are below our detection limits for individual sources will contribute to the diffuse component observed in an image. To examine the potential importance of such an effect, we have taken advantage of the optical WFPC2 image of NGC 2997. The optical image reveals many more sources, especially faint ones, than the FOC UV image. This could be because of the better resolution (and hence sensitivity to faint objects) of the un-aberrated optical image, or because the fainter sources are intrinsically redder (due, e.g., to age or reddening of a cluster) and hence invisible in the UV, or a combination of both.

To study this question we performed the following simulation. We convolved the WFPC2 optical image with the spherically-aberrated PSF, and scaled the resulting image so that 10 of the medium-brightness clusters would have similar counts to those measured in the FOC UV image. After subtracting a constant to make the background similar to that measured in the FOC image, we added Poisson noise, and so obtained a simulated FOC image of how the galaxy would appear if all the compact sources had a UV-optical color similar to that of the medium-bright clusters. We find that, in fact, the simulated FOC image is similar to the actual observed one, with most of the faint optical sources undetectable. This indicates that, at least in this galaxy, the actual fraction of the UV light coming from clusters could be larger than measured (14%), simply due to the lower sensitivity of the UV setup. Since 60% of the light from compact sources in the optical image is from sources that are undetected in the UV image, the true fraction of the UV light contributed by compact sources could be as high as $2.5 \times 14\% = 35\%$. If such a factor applies to the other galaxies as well, the corrected fraction there will be as high as $\sim 50\%$. Alternatively, the assumption of similar color for all clusters may be wrong, and the faint objects may be undetected in the UV because they are too red. If so, the measured UV fraction in clusters is representative of the true fraction. This question can be resolved by deeper UV observations of these galaxies with the now-repaired *HST* optics. In any case, the contribution of the clusters to the UV light is substantial, reaching nearly one-half in NGC 1512.

4.2. The Nature of the Compact Sources

In the previous studies that have reported UV observations of super star clusters, or observations of clusters in nuclear rings, data at the *HST* angular resolution were obtained

in only one broad band per galaxy. Calculations of the extinction-corrected luminosity and color of the clusters depended on extinction factors derived from ground-based imaging and spectroscopy having much lower angular resolution than the *HST* data. These corrections are uncertain in view of the heterogeneous mixture of stars, clusters, and dust seen in the *HST* images. It is also conceivable that the detected clusters are selectively those that are least obscured. In the absence of reliably de-reddened luminosity and color information, a discussion of the masses and ages, and hence nature of the clusters, is speculative. While the data for four of the five galaxies presented here suffer from the same single-band problem, the UV and optical images of NGC 2997 offer us the opportunity for the most detailed examination to date of the nature of the clusters.

Using the fluxes in Table 5, we list in Table 7 for every compact source in NGC 2997 that is detected in both the optical and the UV images a 6000 Å – 2300 Å color and an observed luminosity. We relate these observables to the reddening, mass, and age of each cluster by calculating stellar cluster synthesis and evolution models, as described by Krabbe et al. (1994) and by Kovo & Sternberg (1996). Briefly, we assume an initial mass function (IMF), a star formation rate, and its functional dependence on time (e.g., a constant, continuous rate of star formation, or an exponentially decreasing burst with some characteristic decay time). The evolution of the luminosity and broad-band spectrum of the different stellar types are traced using solar-metallicity Geneva stellar tracks (Schaller et al. 1992). The broad-band properties are weakly dependent on metallicity (e.g., Leitherer & Heckman 1995). For any input IMF (including slope, and upper and lower mass cutoffs), star formation rate, and cluster age, the integrated luminosity at any wavelength and the total stellar mass can be computed. "Color-color" and "color-magnitude" diagrams can thus be produced, the effects of reddening by a chosen extinction law can be applied to the calculation, and the results compared to the observations.

Our models are similar to those presented in the literature by several investigators (e.g., Larson & Tinsley 1978; Mas Hesse & Kunth 1991; Bruzual & Charlot 1993; Vacca 1994; Leitherer & Heckman 1995). We have compared our model results with those of Leitherer & Heckman (1995) and find good agreement. For example, our computed V magnitudes agree well (generally to within 0.3 magnitudes) with those of Leitherer & Heckman for both continuous and decaying bursts and a range of IMF slopes and upper mass cut-offs.

Figure 4 shows a "color-magnitude" diagram resulting from such a calculation, relating the 6000 Å luminosity to the 6000 Å – 2300 Å color. The two trajectories show how two clusters of two different total masses move on the diagram with time (the total mass simply scales with the luminosity). We have assumed an IMF with a power-law slope of -2.5, upper and lower stellar mass cutoffs of $30 M_\odot$ and $1 M_\odot$, and an exponentially decreasing

star formation rate with characteristic time 5 Myr. The total cluster mass is that which is reached asymptotically. The points plotted in Figure 4 give the color and luminosity of all the NGC 2997 clusters detected in both bands, as listed in Table 7. The arrow in Fig. 4 shows the de-reddening vector for an extinction law [4] of the form $A_\lambda \propto \lambda^{-1}$ mag. A visual extinction $A_V = 0.3$ is expected for NGC 2997 from foreground Galactic absorption alone (Burstein & Heiles 1982).

Several inferences can be made from Figure 4, given the assumptions regarding the IMF and the burst-like star formation rate. If the clusters are unreddened, their total masses are between a few thousand and $10^5 M_\odot$, and their ages are 10 to 100 Myr. A de-reddening correction will move the points leftward (bluer) and upward (higher luminosity) on the plot. Therefore, the ages of the clusters, as read off the plot, are upper limits to the true ages. *All 24 clusters detected in both bands are younger than* ~ 100 *Myr.* Similarly, the masses obtained from the plot are lower limits to the true masses. *Most of the clusters have masses* $\gtrsim 10^4 M_\odot$. A de-reddening correction will move the points by about half a decade in luminosity for every decade in color. The reddest clusters can be moved leftward by about one decade, and most clusters by only about half a decade, before they become bluer than a newly-formed cluster of stars. The corollary is that *the clusters seen in both bands are extinguished by, at most, about 1 mag in the visual*, and the mass estimates given above for the unreddened case can be off by a factor of a few, at most.

The above conclusions suggest that the compact sources seen in NGC 2997 are indeed young clusters of stars. The typical radius of these objects is $\lesssim 3$ pc. If there is little reddening, and the true ages of the clusters are close to the upper limits (i.e. tens of Myrs), then the clusters appear to be bound – otherwise they would not have remained compact for so long. For example, for an unbound cluster to retain a 3 pc radius for 25 Myr, the velocity dispersion would have to be less than 0.12 km s^{-1}. The density of the clusters is two orders of magnitude greater than the galaxy density within the ring, so the clusters will not be tidally disrupted. Our results are therefore consistent with the idea that the clusters will evolve into objects similar to present-day globular clusters.

Do these conclusions hold if the clusters are reddened, and hence very young? If a cluster of mass M and radius R is unbound, its velocity dispersion v is

$$v > (2GM/R)^{1/2},$$

---

[4]Meurer et al. (1995) have studied in detail the effects of four different Galactic and extragalactic reddening laws on measurements through the FOC F220W filter. They show that three of the four give $A_{2300} \approx (8.25 \pm 0.25)E(B - V)$ for $0 < E(B - V) < 0.5$ mag, as one would expect from a simplistic $A_\lambda \propto \lambda^{-1}$ model.

and so its maximal age is

$$t_{max} < R/v < 3 \times 10^4 \text{yr} \left(\frac{R}{\text{pc}}\right)^{3/2} \left(\frac{M}{10^5 M_\odot}\right)^{-1/2}.$$

It is unlikely that all the clusters around the ring are only a few tens of thousands of years old. Such instantaneous triggering is difficult to envisage in a ring whose dynamical time scale is $\sim 10^7$ yr (based, e.g., on the kinematics we have measured for the NGC 1079 ring, §3.1). The clusters are therefore bound, even if they are reddened.

How sensitive are these conclusions to the initial conditions of the population synthesis calculation? We find that the curves in the color-magnitude diagram have the same general shape for a star-forming-rate decay time of 1 Myr, rather than 5 Myr, although the trajectories are slightly more jagged at early times due to variations in the post-main-sequence evolution of stars of different masses. For completeness, Figure 5 shows the same kind of calculation, but with a continuous, constant star-formation rate, rather than an exponentially-decaying burst. The two curves show the evolution of a cluster for two star formation rates, $5 \times 10^{-4} M_\odot$ yr^{-1} and $5 \times 10^{-5} M_\odot$ yr^{-1}. In this case, the total mass in a cluster is just the star-formation rate times the age of the cluster, and so is not constant. As can be seen, under the continuous star-formation assumption the ages of the clusters in NGC 2997 could be up to ~ 500 Myr, since the observed blue color is provided by young stars, which are constantly produced in a cluster. However, such a star-formation scenario is probably unrealistic, as it requires stars to be formed only in select regions of radius 3 pc for 500 Myr (~ 50 orbital periods). The first supernovae would probably blow away much of the gas in such a small region, so continuous accretion from the surrounding ISM is required. The continuous star-formation scenario is less problematic if the clusters are reddened, and so can be moved in Figure 5 to lower ages.

We find the model calculations are only weakly affected if, instead of an IMF slope of -2.5, we use a Salpeter (1955) slope of -2.35. This approximate slope has been observed in a variety of star-forming environments (e.g., Lada et al. 1991; Lada & Lada 1995). The results are also weakly sensitive to the upper mass cutoff of the IMF, since the most massive stars live for a very short time before exploding and disappearing. Raising the lower mass cutoff would not change the observables plotted in Figures 4-5, since the UV light is dominated by massive main-sequence stars, while about half the optical light is contributed by red giants that have evolved from intermediate-mass stars and the rest by massive main-sequence stars. The total cluster mass, most of which is in low-mass stars on the main sequence, would increase by a factor of ~ 2 or decrease by a factor of ~ 3 if the low-mass cutoff were at $0.1 M_\odot$ or $5 M_\odot$, respectively, instead of at $1 M_\odot$.

In fact, it has been claimed (Rieke et al. 1980, 1993) that the IMF in the starburst

galaxy M82 is deficient in low-mass stars. (This conclusion is, however, controversial; see Scalo 1986.) Since much of the unobscured star formation in M82 takes place in super star clusters (O'Connell et al. 1995), they could be the site of this deficiency. If the same mechanism operates in NGC 2997, its clusters would be different from present-day globulars, in terms of mass function. The masses and stellar content of the ring clusters are still uncertain and can be constrained by observations at additional bands, which can disentangle the effects of reddening and age.

The range of UV luminosities of the clusters in the four other galaxies presented here is similar to that of NGC 2997. In the absence of information at other wavebands, the masses and ages of the clusters are degenerate, even without the assumptions about the IMF, the star-formation history, and the extinction. From our models, we find that the cluster mass dependence on the UV luminosity and the age, after $t \gtrsim 10^7$yr, can be parametrized with the following power laws. For the model described above, with an exponentially-decaying star formation rate,

$$M = 3 \left(\frac{L_\lambda(2270\text{Å})}{10^{33} \text{ erg s}^{-1}\text{Å}^{-1}} \right) \left(\frac{t}{10^7\text{yr}} \right)^{1.43} M_\odot.$$

For the continuous star-forming model,

$$M = 2 \left(\frac{L_\lambda(2270\text{Å})}{10^{33} \text{ erg s}^{-1}\text{Å}^{-1}} \right) \left(\frac{t}{10^7\text{yr}} \right)^{0.83} M_\odot.$$

The UV properties of the other four galaxies are similar in all respects to those for NGC 2997. It is therefore likely that the conclusions regarding the age, mass, and reddening of the clusters in NGC 2997 will apply to those galaxies as well, once data in additional bands are obtained for them.

4.3. The Cluster Luminosity Function

Several of the previous *HST* studies that have detected super star clusters have also measured their luminosity functions. Meurer et al. (1995) find that the combined luminosity function $N(L)$ of the clusters they measure in most of their starburst galaxies has a power-law shape, $N(L)dL \propto L^\alpha dL$, with slope $\alpha \approx -2$. Whitmore & Schweizer (1995) fit a power law of similar slope to the cluster luminosity function of the merging system NGC 4038/4039. The luminosity function shown by Barth et al. (1995) for the clusters in the circumnuclear ring in NGC 1097 is also consistent with a power-law distribution of slope approximately -2.

It is interesting to see if the same luminosity function persists in additional examples of clusters in the circumnuclear ring environment. Indeed, the luminosity function of the clusters in each of the five galaxies peaks near the detection limit, and falls off at higher luminosities. However, the numbers are small. Figure 6 shows the combined luminosity function for NGC 1433, NGC 1512, and NGC 2997. These three galaxies are all at a similar distance (~ 10 Mpc), so the cluster detection limit is at a similar luminosity ($\log L_\lambda(2270\text{Å}) \approx 34.5$). The detection limit should then not affect the shape of the combined luminosity function at luminosities above it. Figure 6 compares the luminosity function to a power law of slope -2 (the dashed line, which has slope -1 in logarithmic intervals of L). Within the limitations of the small numbers, for $\log L_\lambda(2270\text{Å}) \geq 35.5$ the luminosity function of the ring clusters appears to follow the same $\alpha = -2$ power law observed for clusters in other environments and at other wavebands. Note that Meurer et al. (1995) plot the cluster luminosity function only for clusters brighter than absolute magnitude (as defined by them) $M_{220} = -14$. This magnitude, which is their defining limit for super star clusters, corresponds to $\log L_\lambda(2270\text{Å}) > 37.25$. Our result shows that this power law shape also describes the luminosity function at luminosities lower by 1-2 orders of magnitude. (However, the comparison is not straightforward, because Meurer et al. (1995) have attempted to correct their cluster luminosities for extinction, whereas we have not.)

The $\alpha = -2$ power law overpredicts by a factor of 2 the number of clusters in the $34.9 \leq \log L_\lambda(2270\text{Å}) \leq 35.3$ bin. A source at $D = 10$ Mpc with $\log L_\lambda(2270\text{Å})$ in this range produces 250-600 total counts in our FOC exposures. Such sources, although conspicuous if isolated, can be difficult to detect on a high background or in the neighborhood of brighter sources. We suspect that the low number of clusters in this luminosity bin is the result of this detection problem, rather than a real turnover in the luminosity function.

4.4. The Occurrence of Circumnuclear Rings

While there are some theoretical explanations for the occurrence of circumnuclear rings (see §1), and detailed modeling of individual cases, there have been few statistics on the circumstances under which these rings appear. Our sample provides a good opportunity to study the statistics of nuclear ring formation because
(1) the ringed galaxies were identified from an unbiased sample drawn from a complete, diameter-selected galaxy sample;
(2) the *HST* resolution allows detection of small rings that would have been missed from the ground (e.g. NGC 1079); and
(3) the UV bandpass emphasizes these star-forming structures over the optically-bright but

UV-dark central regions of a galaxy, again aiding in detection.
On the other hand, the small field of view of the FOC will exclude large, face-on nuclear rings in the more nearby galaxies, and dusty nuclear rings will pass undetected in the UV.

To check the effectiveness of the UV images in detecting nuclear rings, we have examined the FOC images of all the galaxies in our sample appearing in the compilation of known nuclear rings by Buta & Crocker (1993). There are seven such galaxies. Four of the seven are the previously-known ring galaxies discussed in this paper. Two of the seven (NGC 1543 and NGC 3486) have nuclear rings larger than the FOC field of view, explaining why we did not detect them as such. One of the seven (NGC 2903) is described by Pogge (1989) as an "incomplete" nuclear ring. He shows an Hα image of the galaxy, consisting mostly of an extended knot to one side of the nucleus. The *HST* F220W image of the galaxy shows a large number of super star clusters whose geometry matches up with the gross features in Pogge's ground-based image. The geometry of the clusters is, however, too random to be classified as a ring. This galaxy will be analyzed further in Ho et al. (1996c). We conclude that our UV images are effective at detecting nuclear rings when their angular scale fits on the FOC field of view.

Models have generally involved the influence of bars in the formation of circumnuclear rings. In the RC3 (de Vaucouleurs et al. 1991) catalog, all five of the galaxies discussed here are classified as barred (SB or SAB). For comparison, 52 of the 103 galaxies observed in the *HST* sample are classified as barred by RC3. Our data therefore suggest that barred galaxies are the preferred sites of nuclear ring formation. There are, however, known examples of nuclear rings in unbarred galaxies, such as NGC 7742 (Pogge & Eskridge 1993; Wakamatsu et al. 1996). Our statistics also suggest that at least 5/52, or about 10%, of galaxies with large-scale bars have a circumnuclear ring.

The five galaxies in the sample that have nuclear rings range in morphological type from S0 to Sc. Figure 7 shows the distribution of morphological types among the entire galaxy sample and the five ring galaxies, using the RC3 classification. There is no clear preference for a particular morphological type, but there is a trend toward earlier types.

4.5.   The Active Nucleus Connection

The occurrence of circumnuclear rings may be connected to bar-driven inflow. One of the outstanding problems in the theory of active galactic nuclei (AGNs) is the mechanism that drives galactic material, with its large angular momentum, to the nucleus and into the postulated massive black hole (see, e.g., Phinney 1994). AGNs, bars, and circumnuclear

rings co-exist in some galaxies. It has been speculated that there is perhaps an AGN in the center of every ring, possibly as the result of the same infall-driving mechanism (e.g., Dultzin-Hacyan 1995). On the other hand, a correlation could simply be the result of the fact that rings tend to occur in early-type galaxies, which are the preferred sites of LINER and Seyfert-type AGNs (e.g., Ho et al. 1996a). The absence of a bar-AGN connection is demonstrated by Ho, Filippenko, & Sargent (1996b), who show that AGNs are equally likely to occur in barred and unbarred galaxies.

Our sample allows a statistical examination of the nuclear-ring/AGN connection. Among the low ionization nuclear emission-line regions (LINERs; Heckman 1980) and Seyfert galaxies in the northern galaxies of the sample (Maoz et al. 1995; Maoz 1996), none has a circumnuclear ring detected in the UV. Based on spectral classifications from the literature, none of the five detected ring galaxies has a LINER or Seyfert spectrum. The latter fact needs confirmation using high resolution and high-S/N spectroscopy that may reveal faint AGN emission lines on the stellar background, through apertures that will effectively exclude light from the rings. Since four of the five ring galaxies are in the South, spectral classification of the nuclei of all the southern galaxies in the *HST* sample would enable further testing for connections between rings and AGNs. Tentatively, we conclude that, although examples of co-existing rings and AGNs are known (e.g., NGC 1097 and NGC 6951; Barth et al. 1995), there is no evidence for a clear correspondence between the two.

5. Conclusions

We have presented *HST* data for five nearby galaxies displaying circumnuclear star-forming rings in the UV. The rings are composed of numerous compact ($<$ few pc) and luminous objects, similar in all respects to those that have been recently seen in other starburst environments and presumed to be young star clusters. One of the galaxies, NGC 2997, has an *HST* image in visual light, providing color information for these objects at the *HST* angular resolution.

We summarize our main conclusions as follows.
1. A substantial fraction (10%–40%) of the UV light in these galactic circumnuclear regions is emitted by the compact sources. Considering our detection limits, the true fraction may be larger, of order 30%–50%. Compact clusters are therefore a common, and possibly dominant mode of star formation in circumnuclear starbursts.
2. In NGC 2997, the typical compact source has the color of a late B to early A star and the luminosity of $\sim 10^4 - 10^5$ such stars, or the luminosity of tens of OB stars. The object

must therefore be either a ~ 30 Myr-old unreddened cluster, or a young reddened cluster. Either way, the mass of the typical object is $\gtrsim 10^4 M_\odot$.

3. The blue color of the NGC 2997 clusters which are visible in both optical and UV bands means that these clusters are not highly reddened, and are absorbed in the UV by less than a factor of 10. From the present data we cannot say whether the clusters that are detected only in the visual band (75% of the total) are fainter than the UV detection limit, more reddened, or older than the others.

4. Most of the clusters with measurable size have radius < 5 pc. When combined with the age or mass estimates above, this implies they are bound, and they will evolve into objects similar to globular clusters.

5. UV-selected circumnuclear rings occur preferentially in barred galaxies of Hubble type S0 to Sc. There is no clear correspondence between their occurrence and that of a Seyfert or LINER-type AGN.

Further observations in additional wavebands at the *HST* resolution can significantly constrain the nature of these objects, and disentangle the effects of age, reddening, and star-forming initial conditions and history.

REFERENCES

Allen, C. W. 1973, Astrophysical Quantities, 3rd Edition, (London: Athlone)

Arp, H., & Sandage, A. 1985, AJ, 90, 1163

Athanassoula, E. 1992, MNRAS, 259, 345

Barth, A. J., Ho, L. C., Filippenko, A. V., & Sargent, W. L. W. 1995, AJ, 110, 1009

Baxter, D. A., Gilmore, D., Greenfield, P. E., Hack, W., Hodge, P., Jedrzejewski, R. I., & Nota, A. 1994, in "HST Data Handbook", ed. S. Baum (Baltimore: STScI)

Benedict, G. F., et al. 1993, AJ, 105, 1369

Brandl, B., et al. 1996, ApJ, in press

Bruzual, G. A., & Charlot, S. 1993 ApJ 405, 538

Burrows, C. J., et al. 1991, ApJ, 369, L21

Burstein, D., & Heiles, C. 1982, AJ, 87, 1165

Burstein, D., Bertola, F., Buson, L. M., Faber, S. M., & Lauer, T. R. 1988, ApJ, 328, 440

Buta, R., & Crocker, D. A. 1993, AJ, 105, 4

Conti, P. S., & Vacca, W. D. 1994, ApJ, 423, L97

de Vaucouleurs, G., de Vaucouleurs, A., Corwin, H. G., Buta, R. J., Paturel, G., & Fouqué, P. 1991, Third Reference Catalog of Bright Galaxies (New York: Springer)

Dultzin-Hacyan, D. 1995, in Proc. of 5th Mex-Tex Conference on Gaseous Nebulae & Star Formation, Rev. Mex. A & A, SC 3, 31

Elmegreen, B. G. 1994, ApJ, 425, L73

Fillmore, J., Boroson, T., & Dressler, A., 1986, ApJ, 302, 208

Heckman, T. M. 1980, A&A, 87, 152

Ho, L. C., Filippenko, A. V., & Sargent, W. L. W. 1995, ApJS, 98, 477

Ho, L. C., Filippenko, A. V., & Sargent, W. L. W. 1996a, ApJ, submitted

Ho, L. C., Filippenko, A. V., & Sargent, W. L. W. 1996b in IAU 157, "Barred Galaxies", ed. R. Buta, B. G. Elmegreen, & D. A. Crocker (San Francisco: ASP), in press

Ho, L. C., et al. 1996c, in preparation

Holtzman, J. A., et al. 1992, AJ, 103, 691

Hummel, E., van der Hulst, J. M., & Keel, W. C. 1987, A&A, 172, 32

Hunter, D. A., O'Connell, R. W., & Gallagher, J. S. 1994, AJ, 108, 84

Kenney, J. D. P., Wilson, C. D., Scoville, N. Z,. Devereux, N. A., & Young, J. S. 1992, ApJ, 395, L79

Kennicutt, R. C. 1994, in Mass Transfer-Induced Activity in Galaxies, ed. I. Shlosman (Cambridge: Cambridge University Press), 131

Kennicutt, R. C., & Chu, Y.-H. 1988, AJ, 95, 720

Kennicutt, R. C., Keel, W. C., & Blaha, C. A. 1989, AJ, 97, 1022

Kinney, A. L., Bohlin, R. C., Calzetti, D., Panagia, N., & Wyse, R. F. G. 1993, ApJS, 86, 5

Kovo, O., & Sternberg, A. 1996, in preparation

Krabbe, A., Sternberg, A., & Genzel, R. 1994, ApJ, 425, 72

Krist, J. 1994, The Tiny Tim User's Manual (Baltimore: STScI)

Lada, E. A., Evans, N.J., Depoy, D. L., & Gatley, I. 1991 ApJ, 371, 171

Lada, E. A., & Lada, C. J. 1995 AJ 109, 1682

Larson, R. B., & Tinsley, B. M. 1978, ApJ, 219, 46

Lauberts, A., & Valentijn, E. A. 1989, "The Surface Photometry Catalogue of the ESO-Uppsala Galaxies" (Garching: ESO)

Leitherer, C., & Heckman, T. M. 1995, ApJS, 96, 9

Maoz, D., Filippenko, A. V., Ho, L. C., Rix, H. -W., Bahcall, J. N., Schneider, D. P., & Macchetto, F. D. 1995, ApJ, 440, 91

Maoz, D. 1996, in "The Physics of LINERs in View of Recent Observations", eds. M. Eracleous et al. (Baltimore: STScI), in press

Maoz, D., Filippenko, A. V., Ho, L. C., Macchetto, F. D., Rix, H.-W., & Schneider, D. P. 1996, ApJS, submitted

Mas Hesse, J. M., & Kunth, D. 1991, A&AS, 88, 399

Mayya, Y. D. 1995, AJ, 108, 1276

Meaburn, J., & Terret, D. L. 1982, MNRAS, 200, 1

Meurer, G. R. 1995a, Instrument Science Report FOC-083 (Baltimore: STScI)

Meurer, G. R. 1995b, Nature, 375, 742

Meurer, G. R., Heckman, T. M., Leitherer, C., Kinney, A., Robert, C., & Garnett, D. R. 1995, AJ, 110, 2665

Melnick, J., Moles, M., & Terlevich, R. 1985, A&A, 149, L24

Miller, J. S., & Stone, R. P. S. 1993, Lick Obs. Tech. Rep., No. 66

Nota, A., Jedrzejewski, R., & Hack W. 1995, "Faint Object Camera Instrument Handbook" (Baltimore: STScI)

O'Connell, R. W., Gallagher, J. S., & Hunter, D. A. 1994, ApJ, 433, 65

O'Connell, R. W., Gallagher, J. S., Hunter, D. A., & Colley, W. N. 1995, ApJ, 446, L1

Paresce, F. 1990, "Faint Object Camera Instrument Handbook" (Baltimore: STScI)

Pogge, R. W. 1989, ApJS, 71, 433

Pogge, R. W., & Eskridge, P. B. 1993, AJ, 106, 1405

Phillips, A. C. 1993, Ph.D. thesis, University of Washington

Phinney, E. S. 1994, in Mass Transfer-Induced Activity in Galaxies, ed. I. Shlosman (Cambridge: Cambridge University Press), p. 1

Piner, B. G., Stone, J. M., & Teuben, P. J. 1995, ApJ, 449, 508

Rieke, G. H., Lebofsky, M. J., Thompson, R. I., Low, F. J., & Tokunaga, A. T. 1980, ApJ, 238, 24

Rieke, G. H., Loken, K., Rieke, M. J., & Tamblyn, P. 1993, ApJ, 412, 99

Rix, H. -W., & White, S. D. M. 1992, MNRAS, 254, 389

Rix, H. -W., Kennicutt, R. C., Braun, R., & Walterbos, R. A. M. 1995, ApJ, 438, 155

Sandage, A., & Bedke, J. 1988, *Atlas of Galaxies Useful for Measuring the Cosmological Distance Scale* (Washington D.C.: NASA), p. 41

Scalo, J. M. 1986, Fund. of Cosmic Phys, 11, 1

Schaller, G., Schaerer, D., Meynet, G., & Maeder, A. 1992, A&AS, 96, 269

Sérsic, J. L., & Pastoriza, M. 1967, PASP, 79, 152

Stetson, P. B. 1987, PASP, 99, 191

Tacconi-Garman, L., Sternberg, A., & Eckart, A. 1996, AJ, submitted

Tubbs, A. D. 1982, ApJ, 255, 458

Tully, R. B. 1988, "Nearby Galaxies Catalog" (Cambridge: Cambridge University Press)

Vacca, W. D. 1994, ApJ, 421, 140

Walsh, J. R., Nandy, K., Thompson, G. I., & Meaburn, J. 1986, MNRAS, 220, 453

Wakamatsu, K., Hamabe, H., Nishida, M. T., & Tomita, A. 1996, in IAU 157, "Barred Galaxies", ed. R. Buta, B. G. Elmegreen, & D. A. Crocker (San Francisco: ASP), in press

Whitmore, B. C., et al. 1993, AJ, 106, 1354

Whitmore, B. C., & Schweizer, F. 1995, AJ, 109, 960
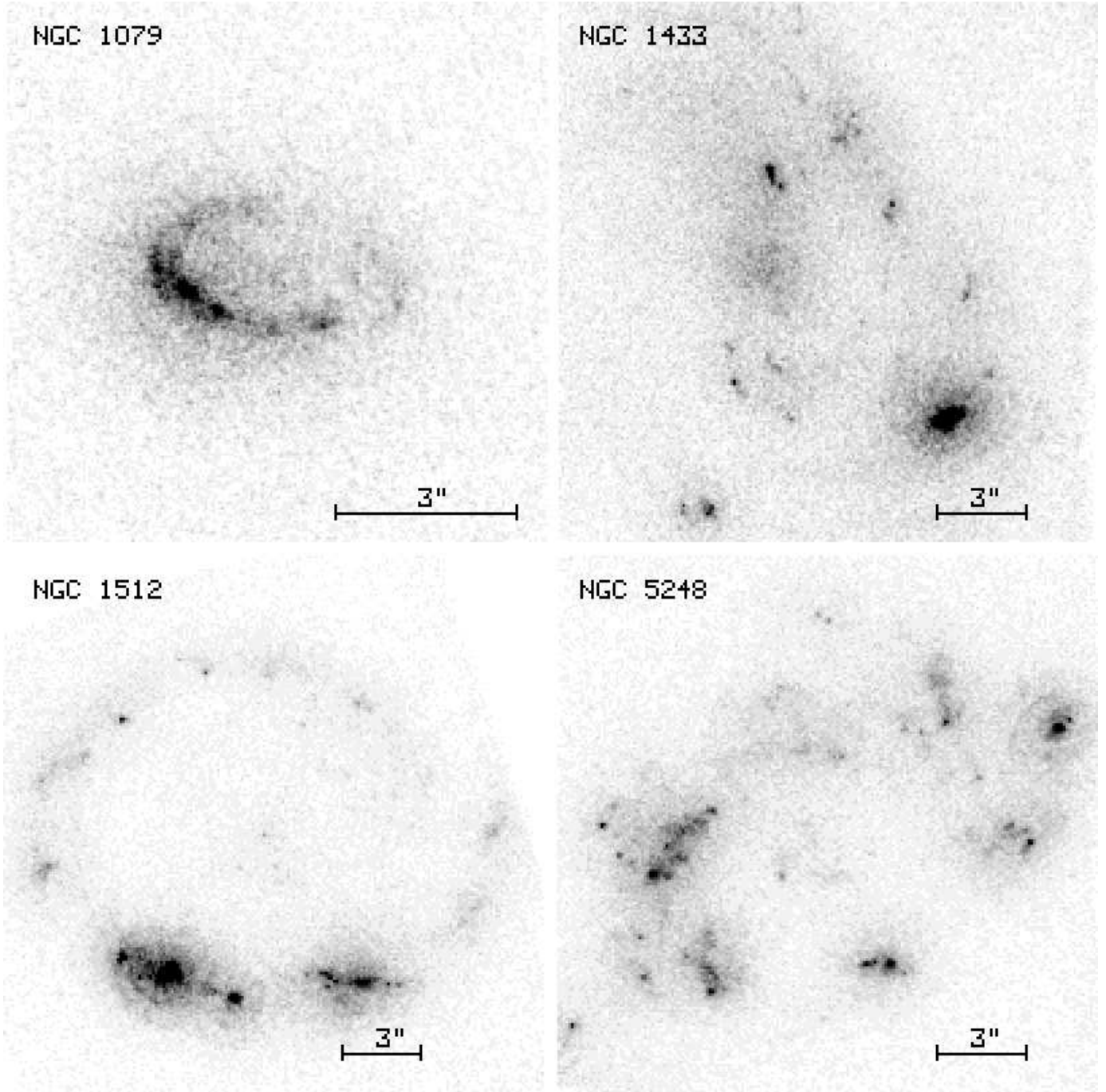
Fig. 1.— *HST* FOC F220W images of four of the circumnuclear rings. North is up and east is to the left. The scale of each image section is marked.
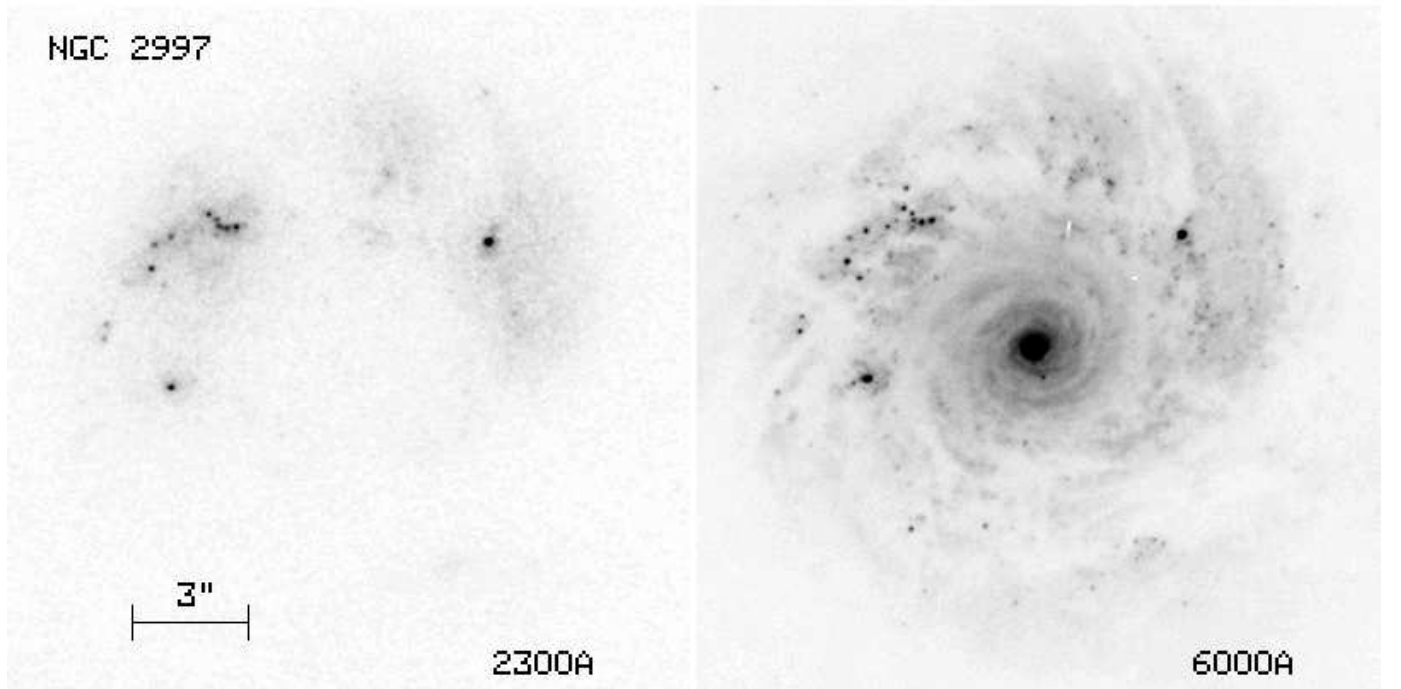
Fig. 2.— *HST* images of the nuclear ring in NGC 2997. Left panel: FOC F220W (UV) image. Right panel: WFPC2 F606W (optical) image, to the same scale. Note the different appearance of the galaxy in the UV image, which highlights only regions of current and recent star formation. North is up, east is to the left.
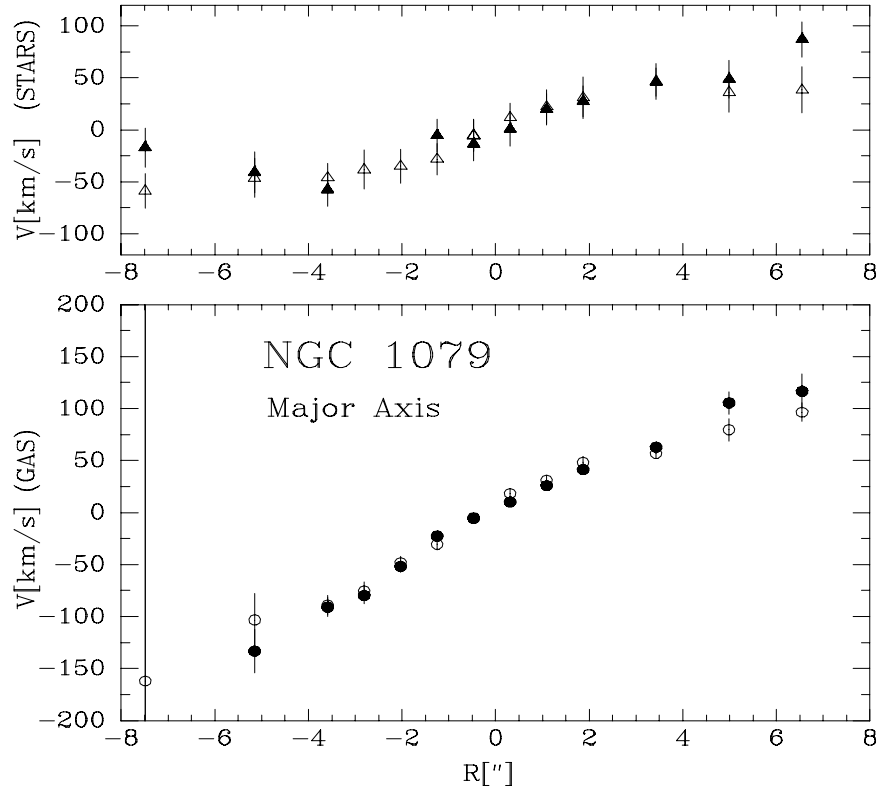
Fig. 3.— Major-axis rotation curves obtained for NGC 1079 using absorption lines, which trace stars (top panel), and emission lines, which trace gas (bottom panel). Filled and empty symbols denote two independent observations.
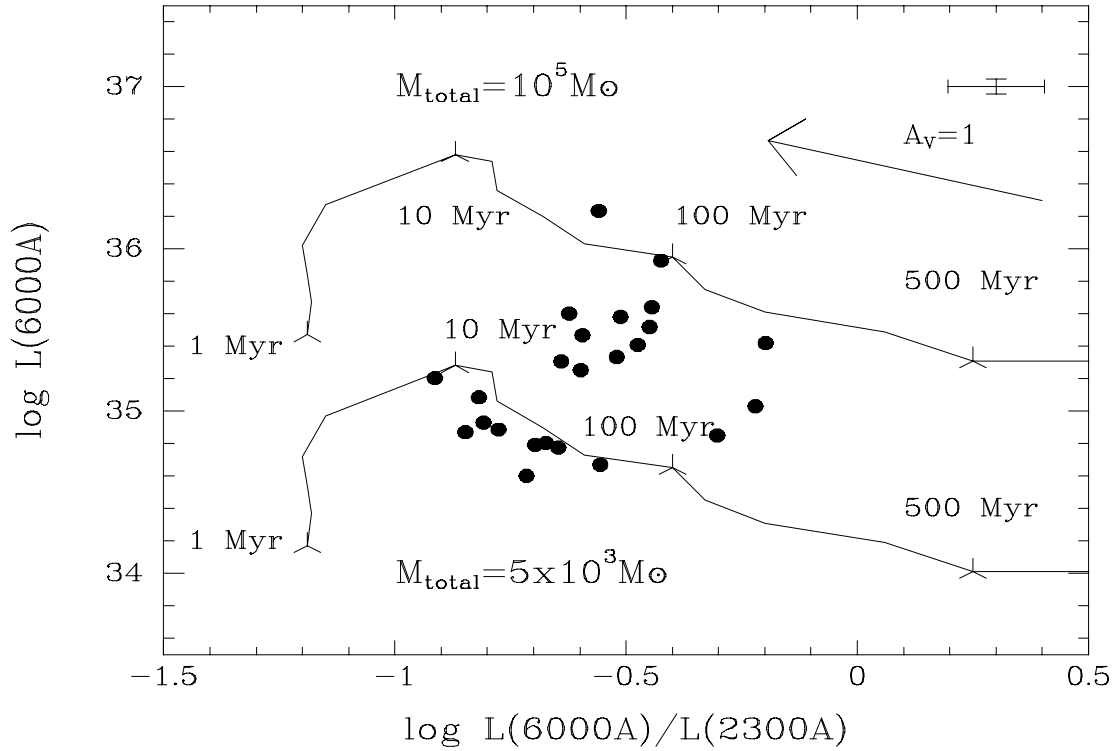
Fig. 4.— Color-magnitude diagram for the clusters in NGC 2997, relating the 6000 Å luminosity to the 6000 Å – 2300 Å color. The points show the color and luminosity of all the NGC 2997 clusters detected in both bands, as listed in Table 7. The two curves show how two clusters of different total mass move on the diagram with time. An exponentially decreasing star formation rate with characteristic decay time of 5 Myr is assumed. Also shown (arrow) is a de-reddening vector, giving the correction for one magnitude of foreground visual extinction, and the typical error bar for an observed point (upper-right corner).
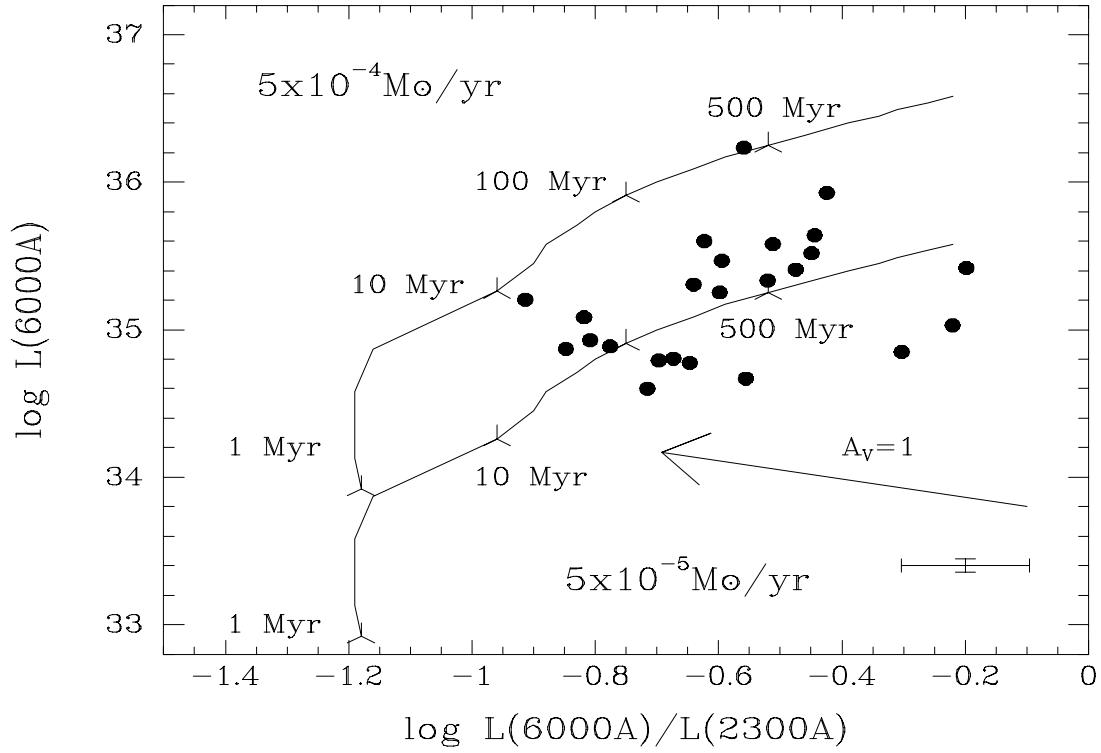
Fig. 5.— As in Fig. 4, but with the modelled evolution of two clusters with a *constant* $(5 \times 10^{-4}$ and $5 \times 10^{-5} M_\odot$ yr$^{-1})$ star formation rate (SFR). The mass of the cluster in stars at a given time is the SFR times the age.
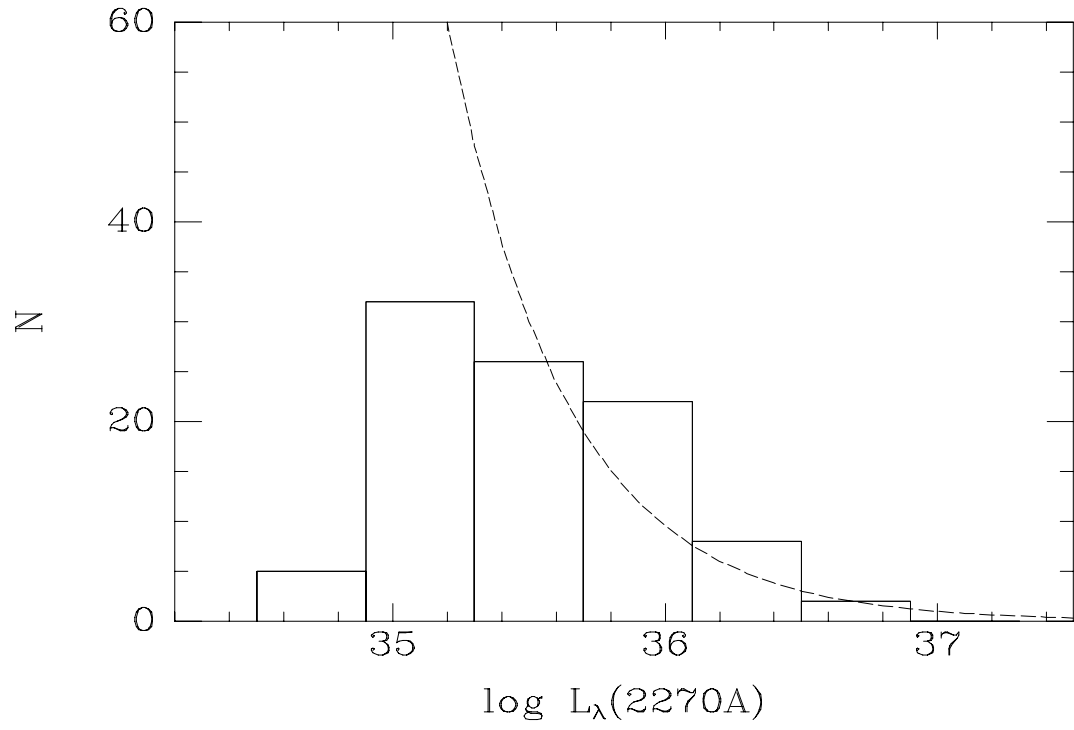
Fig. 6.— Combined observed UV luminosity function for the clusters in NGC 1433, NGC 1512, and NGC 2997. Also plotted (dashed line) is a luminosity function of the form $N \propto L^{-2}$.
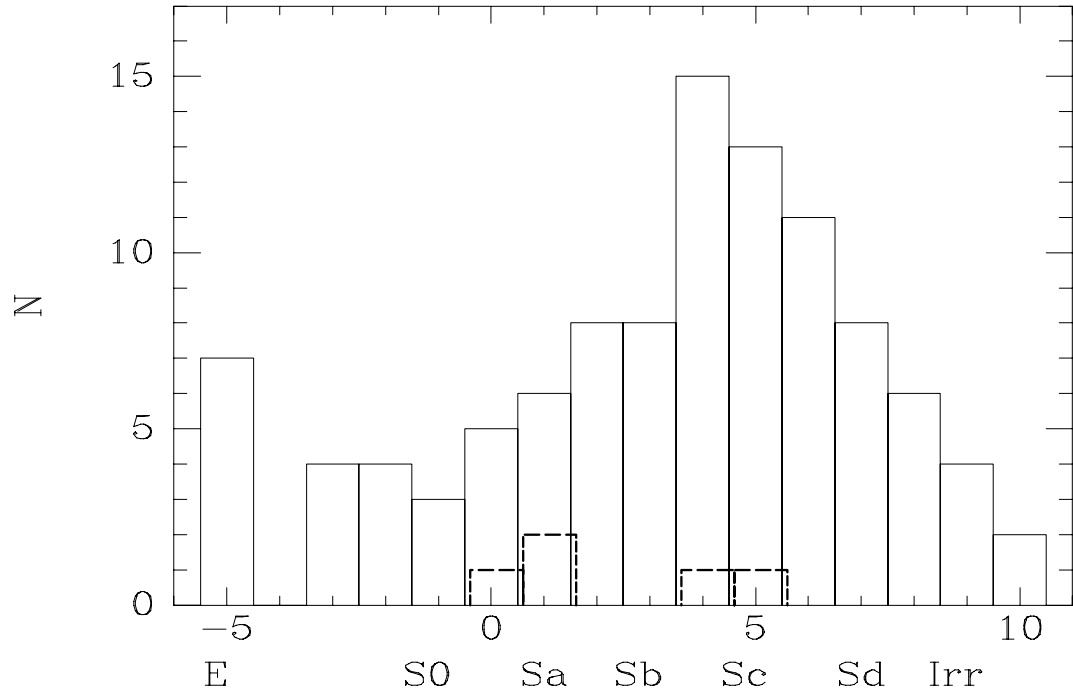
Fig. 7.— The distribution of morphological types among the 103 galaxies in the *HST* survey, and among the five nuclear-ring galaxies (dashed histogram), based on de Vaucouleurs's "T-type" classification.

TABLE 1. Circumnuclear Ring Galaxies

Galaxy	R.A.(J2000)	Decl.(J2000)	Type	Distance (Mpc)	Ring-Diam. (pc)	$f_\lambda(2270\text{Å})$ Total
NGC 1079	$02^h43^m44^s.5$	$-29°00'10''$	SAB0	16.9	330	2.1
NGC 1433	03 42 01.4	-47 13 20	SBab	11.6	540	6.8
NGC 1512	04 03 54.2	-43 20 57	SBab	9.5	690	9.5
NGC 2997	09 45 38.6	-31 11 25	SABc	13.8	540	7.6
NGC 5248	13 37 32.0	$+08$ 53 07	SABbc	22.7	1200	9.7

Notes to Table 1.

Distances from Tully(1988); distances and sizes assume $H_0 = 75$ km s^{-1} Mpc^{-1}; $f_\lambda(2270\text{Å})$ is total flux from ring, in units of 10^{-15} erg s^{-1} cm^{-2} Å^{-1}.

TABLE 2. Compact Sources – NGC 1079

No. (1)	X (2)	Y (3)	$\Delta\alpha('')$ (4)	$\Delta\delta('')$ (5)	$f_\lambda(2270\text{Å})$ (6)	$R('')$ (7)	R (pc) (8)
0	636.0	491.0	0.00	0.00	$\cdots$	$\cdots$	$\cdots$
1	613.1	539.8	0.76	0.95	1.2	$\cdots$	$\cdots$
2	583.5	523.7	1.32	0.44	0.4	$\cdots$	$\cdots$
3	579.9	505.9	1.30	0.03	0.3	$\cdots$	$\cdots$
4	569.1	540.1	1.72	0.73	1.8	$\cdots$	$\cdots$
5	546.5	538.5	2.21	0.57	0.5	$\cdots$	$\cdots$
6	538.3	514.2	2.26	0.00	2.9	0.05	4.2
7	535.1	501.2	2.26	-0.30	1.3	$\cdots$	$\cdots$
8	553.8	496.6	1.83	-0.30	10.2	0.07	5.6
9	557.0	491.6	1.73	-0.40	9.6	0.07	6.0
10	575.1	473.9	1.24	-0.69	6.1	0.05	4.2
11	582.0	467.9	1.06	-0.79	1.4	$\cdots$	$\cdots$
12	593.3	460.4	0.78	-0.89	0.9	$\cdots$	$\cdots$
13	588.1	483.0	1.01	-0.42	0.7	$\cdots$	$\cdots$
14	610.0	453.0	0.37	-0.97	3.7	0.10	8.3
15	647.3	444.2	-0.49	-0.97	4.5	0.10	8.3
16	705.0	447.4	-1.74	-0.60	1.6	$\cdots$	$\cdots$
17	679.1	470.0	-1.05	-0.24	0.6	$\cdots$	$\cdots$
18	686.3	497.3	-1.07	0.40	0.8	$\cdots$	$\cdots$
19	618.8	484.9	0.35	-0.22	0.6	$\cdots$	$\cdots$

Notes to Table 2.

(1) – Source No. 0 denotes the coordinate origin, at the approximate geometrical center of the ring; (2)(3) – X and Y pixel coordinates; (4)(5) – Offset in arseconds from the origin (source No. 0), in the R.A. and Decl. directions; (6) – $f_\lambda(2270\text{Å})$ in units of 10^{-17} erg s^{-1} cm^{-2} Å^{-1}; (7) – σ of best-fit Gaussian width (see text), in arcseconds; (8) – As in (7), assuming distance in Table 1.

TABLE 3. Compact Sources – NGC 1433

No. (1)	X (2)	Y (3)	$\Delta\alpha('')$ (4)	$\Delta\delta('')$ (5)	$f_\lambda(2270\text{Å})$ (6)	$R('')$ (7)	R (pc) (8)
0	674.0	582.0	0.00	0.00	$\cdots$	$\cdots$	$\cdots$
1	284.5	862.6	8.49	6.68	0.7	$\cdots$	$\cdots$
2	539.9	958.6	2.66	8.59	0.5	$\cdots$	$\cdots$
3	503.6	880.5	3.55	6.87	0.6	$\cdots$	$\cdots$
4	547.6	862.4	2.57	6.42	0.7	$\cdots$	$\cdots$
5	625.8	840.2	0.84	5.85	1.1	$\cdots$	$\cdots$
6	632.9	814.8	0.70	5.27	1.9	$\cdots$	$\cdots$
7	612.0	808.2	1.18	5.14	0.7	$\cdots$	$\cdots$
8	612.0	802.1	1.18	5.01	1.0	$\cdots$	$\cdots$
9	605.1	803.9	1.34	5.05	0.9	$\cdots$	$\cdots$
10	596.5	803.6	1.53	5.06	0.9	$\cdots$	$\cdots$
11	506.2	755.4	3.61	4.06	7.6	≤ 0.03	≤ 1.9
12	508.0	745.5	3.58	3.83	3.0	≤ 0.03	≤ 1.9
13	521.2	731.2	3.29	3.50	1.9	$\cdots$	$\cdots$
14	509.6	734.0	3.55	3.57	0.8	$\cdots$	$\cdots$
15	688.1	710.6	-0.44	2.88	2.6	$\cdots$	$\cdots$
16	680.9	695.9	-0.26	2.55	0.9	$\cdots$	$\cdots$
17	681.1	692.0	-0.26	2.47	3.3	0.10	5.7
18	524.2	580.0	3.37	0.10	0.6	$\cdots$	$\cdots$
19	803.9	582.4	-2.92	-0.12	2.4	$\cdots$	$\cdots$
20	465.3	437.9	4.83	-3.04	2.8	0.05	2.9
21	552.4	387.2	2.92	-4.26	2.0	$\cdots$	$\cdots$
22	397.5	252.8	6.53	-7.14	1.0	$\cdots$	$\cdots$
23	395.4	244.8	6.58	-7.31	1.0	$\cdots$	$\cdots$
24	434.2	242.4	5.71	-7.41	2.0	$\cdots$	$\cdots$
25	440.8	251.4	5.56	-7.21	2.6	$\cdots$	$\cdots$
26	752.6	344.0	-1.54	-5.43	0.8	$\cdots$	$\cdots$
27	768.8	393.5	-1.95	-4.33	11.3	0.06	3.2
28	782.6	400.6	-2.27	-4.18	13.7	≤ 0.03	≤ 1.9
29	802.8	406.8	-2.73	-4.06	5.1	0.06	3.2
30	781.5	381.1	-2.23	-4.62	1.7	$\cdots$	$\cdots$
31	787.9	383.9	-2.37	-4.56	3.5	0.10	5.4

Notes to Table 3.

See Table 2 notes

TABLE 4. Compact Sources – NGC 1512

No. (1)	X (2)	Y (3)	$\Delta\alpha('')$ (4)	$\Delta\delta('')$ (5)	$f_\lambda(2270\text{Å})$ (6)	$R('')$ (7)	R (pc) (8)
0	561.0	561.0	0.00	0.00	$\cdots$	$\cdots$	$\cdots$
1	227.2	764.7	8.55	2.07	1.4	$\cdots$	$\cdots$
2	284.9	770.9	7.36	2.60	0.7	$\cdots$	$\cdots$
3	390.3	821.1	5.45	4.40	6.1	0.06	2.6
4	512.4	890.1	3.30	6.72	1.3	$\cdots$	$\cdots$
5	546.2	857.3	2.35	6.25	2.7	$\cdots$	$\cdots$
6	524.6	730.9	1.95	3.39	0.4	$\cdots$	$\cdots$
7	646.6	820.1	-0.05	6.14	1.0	$\cdots$	$\cdots$
8	682.6	720.5	-1.51	4.25	1.1	$\cdots$	$\cdots$
9	780.6	726.9	-3.56	5.06	1.1	$\cdots$	$\cdots$
10	797.6	711.1	-4.04	4.84	1.1	$\cdots$	$\cdots$
11	684.5	637.7	-2.12	2.49	0.4	$\cdots$	$\cdots$
12	559.6	560.8	0.03	-0.01	2.2	$\cdots$	$\cdots$
13	501.9	523.0	1.00	-1.22	0.8	$\cdots$	$\cdots$
14	563.0	504.9	-0.43	-1.19	1.3	$\cdots$	$\cdots$
15	862.5	332.4	-8.03	-2.82	1.2	$\cdots$	$\cdots$
16	828.1	312.1	-7.43	-3.50	1.3	$\cdots$	$\cdots$
17	701.0	246.4	-5.16	-5.78	2.1	$\cdots$	$\cdots$
18	684.6	253.6	-4.76	-5.74	2.0	$\cdots$	$\cdots$
19	666.2	268.6	-4.26	-5.54	1.9	$\cdots$	$\cdots$
20	654.9	269.6	-4.01	-5.60	2.4	$\cdots$	$\cdots$
21	639.3	270.7	-3.67	-5.68	13.6	0.06	2.6
22	594.1	227.5	-3.00	-6.92	1.1	$\cdots$	$\cdots$
23	607.6	259.2	-3.07	-6.14	0.9	$\cdots$	$\cdots$
24	584.2	280.1	-2.43	-5.86	2.7	$\cdots$	$\cdots$
25	600.9	285.9	-2.75	-5.62	3.9	0.06	2.6
26	593.0	296.9	-2.50	-5.44	3.2	≤ 0.03	≤ 1.6
27	588.9	304.9	-2.36	-5.29	2.0	$\cdots$	$\cdots$
28	582.9	307.0	-2.22	-5.29	3.7	0.07	3.4
29	558.0	311.9	-1.65	-5.36	2.4	$\cdots$	$\cdots$
30	516.1	325.5	-0.66	-5.35	0.3	$\cdots$	$\cdots$
31	426.9	311.4	1.16	-6.27	34.5	0.06	2.6
32	399.6	333.5	1.89	-5.98	1.9	$\cdots$	$\cdots$
33	393.9	340.4	2.06	-5.88	0.4	$\cdots$	$\cdots$
34	405.6	393.4	2.18	-4.66	0.7	$\cdots$	$\cdots$
35	342.2	340.7	3.17	-6.22	2.3	$\cdots$	$\cdots$
36	346.7	377.5	3.33	-5.40	6.7	0.04	1.8
37	310.2	376.2	4.10	-5.68	1.1	$\cdots$	$\cdots$
38	300.9	392.9	4.42	-5.39	1.7	$\cdots$	$\cdots$
39	285.6	397.2	4.78	-5.40	3.7	≤ 0.03	≤ 1.6
40	307.2	412.2	4.41	-4.93	0.9	$\cdots$	$\cdots$
41	262.1	432.0	5.52	-4.82	16.5	0.04	1.8
42	267.9	436.1	5.42	-4.69	10.0	0.06	2.6
43	195.9	622.4	8.24	-1.20	3.0	0.07	3.4

Notes to Table 4.

See Table 2 notes

TABLE 5. Compact Sources – NGC 2997

No.	X PC	Y PC	X FOC	Y FOC	$\Delta\alpha('')$	$\Delta\delta('')$	f_λ 6060 Å	f_λ 2270 Å	$R('')$	R (pc)
(1)	(2)	(3)	(4)	(5)	(6)	(7)	(8)	(9)	(10)	(11)
0	540.0	365.0	559.0	471.0	0.00	0.00	$\cdots$	$\cdots$	$\cdots$	$\cdots$
1	649.0	133.2	$\cdots$	$\cdots$	3.56	11.01	0.4	$\cdots$	$\cdots$	$\cdots$
2	425.7	145.9	$\cdots$	$\cdots$	−6.34	9.19	0.1	$\cdots$	$\cdots$	$\cdots$
3	780.1	150.0	$\cdots$	$\cdots$	9.51	10.99	0.3	$\cdots$	$\cdots$	$\cdots$
4	496.9	176.2	$\cdots$	$\cdots$	−2.99	8.23	0.1	$\cdots$	$\cdots$	$\cdots$
5	475.7	203.2	268.9	669.9	−3.78	6.91	0.3	2.0	$\cdots$	$\cdots$
6	473.8	212.1	$\cdots$	$\cdots$	−3.82	6.50	0.1	$\cdots$	$\cdots$	$\cdots$
7	509.9	221.9	$\cdots$	$\cdots$	−2.15	6.27	0.2	$\cdots$	$\cdots$	$\cdots$
8	504.1	226.2	$\cdots$	$\cdots$	−2.39	6.04	0.2	$\cdots$	$\cdots$	$\cdots$
9	525.7	228.8	296.1	558.9	−1.41	6.05	0.3	1.3	$\cdots$	$\cdots$
10	547.1	230.3	$\cdots$	$\cdots$	−0.44	6.10	0.6	$\cdots$	$\cdots$	$\cdots$
11	744.7	237.1	$\cdots$	$\cdots$	8.42	6.90	0.4	$\cdots$	$\cdots$	$\cdots$
12	519.8	239.1	316.6	566.2	−1.61	5.55	0.5	0.8	$\cdots$	$\cdots$
13	545.0	241.0	$\cdots$	$\cdots$	−0.48	5.61	0.1	$\cdots$	$\cdots$	$\cdots$
14	594.4	241.8	$\cdots$	$\cdots$	1.73	5.85	0.6	$\cdots$	$\cdots$	$\cdots$
15	586.9	253.1	$\cdots$	$\cdots$	1.46	5.30	0.3	$\cdots$	$\cdots$	$\cdots$
16	512.1	253.1	$\cdots$	$\cdots$	−1.88	4.88	0.1	$\cdots$	$\cdots$	$\cdots$
17	516.8	253.8	$\cdots$	$\cdots$	−1.66	4.88	0.2	$\cdots$	$\cdots$	$\cdots$
18	525.8	257.7	351.9	546.9	−1.24	4.76	0.3	2.2	$\cdots$	$\cdots$
19	545.7	259.0	$\cdots$	$\cdots$	−0.35	4.81	0.4	$\cdots$	$\cdots$	$\cdots$
20	449.0	259.3	$\cdots$	$\cdots$	−4.66	4.25	0.2	$\cdots$	$\cdots$	$\cdots$
21	530.6	259.9	$\cdots$	$\cdots$	−1.01	4.68	0.3	$\cdots$	$\cdots$	$\cdots$
22	491.3	261.0	$\cdots$	$\cdots$	−2.76	4.41	0.2	$\cdots$	$\cdots$	$\cdots$
23	455.1	261.2	$\cdots$	$\cdots$	−4.38	4.20	0.1	$\cdots$	$\cdots$	$\cdots$
24	547.6	261.8	$\cdots$	$\cdots$	−0.24	4.69	0.3	$\cdots$	$\cdots$	$\cdots$
25	508.9	263.1	$\cdots$	$\cdots$	−1.97	4.42	1.0	$\cdots$	$\cdots$	$\cdots$
26	531.7	263.9	$\cdots$	$\cdots$	−0.94	4.51	0.4	$\cdots$	$\cdots$	$\cdots$
27	$\cdots$	$\cdots$	401.8	697.6	−4.72	4.03	$\cdots$	0.4	$\cdots$	$\cdots$
28	530.2	264.8	$\cdots$	$\cdots$	−1.01	4.46	0.5	$\cdots$	$\cdots$	$\cdots$
29	$\cdots$	$\cdots$	372.0	532.2	−0.95	4.32	$\cdots$	2.5	$\cdots$	$\cdots$
30	631.2	265.2	$\cdots$	$\cdots$	3.50	5.01	0.2	$\cdots$	$\cdots$	$\cdots$
31	385.9	267.2	$\cdots$	$\cdots$	−7.44	3.55	0.3	$\cdots$	$\cdots$	$\cdots$
32	$\cdots$	$\cdots$	407.9	685.4	−4.46	3.86	$\cdots$	0.8	$\cdots$	$\cdots$
33	509.5	269.8	$\cdots$	$\cdots$	−1.90	4.12	0.3	$\cdots$	$\cdots$	$\cdots$
34	639.0	272.2	$\cdots$	$\cdots$	3.90	4.74	0.2	$\cdots$	$\cdots$	$\cdots$
35	506.7	272.8	$\cdots$	$\cdots$	−2.01	3.97	0.2	$\cdots$	$\cdots$	$\cdots$
36	$\cdots$	$\cdots$	341.2	345.9	3.29	4.60	$\cdots$	0.3	$\cdots$	$\cdots$
37	411.6	276.1	$\cdots$	$\cdots$	−6.24	3.30	0.4	$\cdots$	$\cdots$	$\cdots$
38	460.2	279.2	427.0	665.0	−4.05	3.43	0.5	3.4	0.08	5.3
39	650.3	279.7	$\cdots$	$\cdots$	4.44	4.47	0.3	$\cdots$	$\cdots$	$\cdots$
40	513.4	280.1	$\cdots$	$\cdots$	−1.67	3.68	0.1	$\cdots$	$\cdots$	$\cdots$
41	642.2	281.2	$\cdots$	$\cdots$	4.09	4.36	0.3	$\cdots$	$\cdots$	$\cdots$
42	626.7	281.2	$\cdots$	$\cdots$	3.40	4.27	1.0	$\cdots$	$\cdots$	$\cdots$
43	612.2	284.4	$\cdots$	$\cdots$	2.77	4.05	0.2	$\cdots$	$\cdots$	$\cdots$
44	614.6	285.8	$\cdots$	$\cdots$	2.88	4.00	0.2	$\cdots$	$\cdots$	$\cdots$

TABLE 5. (continued)

No.	X PC	Y PC	X FOC	Y FOC	$\Delta\alpha('')$	$\Delta\delta('')$	f_λ 6060 Å	f_λ 2270 Å	$R('')$	R (pc)
(1)	(2)	(3)	(4)	(5)	(6)	(7)	(8)	(9)	(10)	(11)
45	416.9	286.2	$\cdots$	$\cdots$	-5.95	2.87	0.2	$\cdots$	$\cdots$	$\cdots$
46	463.0	288.1	443.0	655.8	-3.87	3.05	7.3	26.4	0.03	2.3
47	$\cdots$	$\cdots$	379.9	386.1	2.30	3.82	$\cdots$	1.3	$\cdots$	$\cdots$
48	479.9	289.1	$\cdots$	$\cdots$	-3.12	3.09	0.3	$\cdots$	$\cdots$	$\cdots$
49	$\cdots$	$\cdots$	369.0	322.0	3.76	3.92	$\cdots$	0.5	$\cdots$	$\cdots$
50	599.2	290.0	$\cdots$	$\cdots$	2.22	3.72	0.7	$\cdots$	$\cdots$	$\cdots$
51	$\cdots$	$\cdots$	412.7	510.2	-0.55	3.36	$\cdots$	0.5	$\cdots$	$\cdots$
52	407.2	291.0	$\cdots$	$\cdots$	-6.35	2.60	0.2	$\cdots$	$\cdots$	$\cdots$
53	568.6	291.1	$\cdots$	$\cdots$	0.86	3.50	0.2	$\cdots$	$\cdots$	$\cdots$
54	$\cdots$	$\cdots$	419.1	529.5	-1.00	3.26	$\cdots$	0.7	$\cdots$	$\cdots$
55	504.0	291.6	$\cdots$	$\cdots$	-2.02	3.12	0.3	$\cdots$	$\cdots$	$\cdots$
56	457.6	292.3	$\cdots$	$\cdots$	-4.09	2.83	0.6	$\cdots$	$\cdots$	$\cdots$
57	434.0	292.9	$\cdots$	$\cdots$	-5.14	2.67	0.2	$\cdots$	$\cdots$	$\cdots$
58	626.8	293.2	378.3	332.8	3.47	3.74	1.4	3.9	0.03	2.3
59	705.1	295.4	$\cdots$	$\cdots$	6.98	4.08	0.3	$\cdots$	$\cdots$	$\cdots$
60	621.7	295.8	386.5	341.6	3.25	3.59	0.9	3.0	0.03	2.3
61	465.7	296.0	$\cdots$	$\cdots$	-3.71	2.71	0.3	$\cdots$	$\cdots$	$\cdots$
62	$\cdots$	$\cdots$	395.9	374.1	2.53	3.44	$\cdots$	1.6	$\cdots$	$\cdots$
63	532.5	298.2	430.2	514.6	-0.72	2.99	0.3	1.3	$\cdots$	$\cdots$
64	609.8	298.3	396.4	363.8	2.74	3.42	1.7	7.1	0.05	3.0
65	449.3	299.0	$\cdots$	$\cdots$	-4.42	2.48	0.4	$\cdots$	$\cdots$	$\cdots$
66	403.2	299.3	$\cdots$	$\cdots$	-6.48	2.21	0.6	$\cdots$	$\cdots$	$\cdots$
67	620.1	299.4	393.4	342.4	3.20	3.42	0.9	3.8	0.04	2.6
68	456.5	299.4	$\cdots$	$\cdots$	-4.10	2.50	0.4	$\cdots$	$\cdots$	$\cdots$
69	615.2	300.0	396.4	352.8	2.99	3.37	1.6	5.2	0.05	3.4
70	630.1	301.0	$\cdots$	$\cdots$	3.66	3.41	0.4	$\cdots$	$\cdots$	$\cdots$
71	597.4	301.2	407.2	387.1	2.20	3.21	0.2	0.9	$\cdots$	$\cdots$
72	495.9	302.3	$\cdots$	$\cdots$	-2.33	2.60	0.5	$\cdots$	$\cdots$	$\cdots$
73	454.1	302.5	$\cdots$	$\cdots$	-4.19	2.35	0.3	$\cdots$	$\cdots$	$\cdots$
74	620.2	303.7	$\cdots$	$\cdots$	3.23	3.23	0.7	$\cdots$	$\cdots$	$\cdots$
75	634.8	305.1	$\cdots$	$\cdots$	3.89	3.25	0.8	$\cdots$	$\cdots$	$\cdots$
76	602.7	307.6	$\cdots$	$\cdots$	2.47	2.96	0.3	$\cdots$	$\cdots$	$\cdots$
77	647.0	309.0	399.7	286.0	4.46	3.15	1.2	4.9	0.04	2.6
78	464.8	309.1	$\cdots$	$\cdots$	-3.68	2.12	0.3	$\cdots$	$\cdots$	$\cdots$
79	$\cdots$	$\cdots$	477.2	650.0	-3.82	2.23	$\cdots$	0.7	$\cdots$	$\cdots$
80	723.3	310.1	$\cdots$	$\cdots$	7.87	3.52	0.2	$\cdots$	$\cdots$	$\cdots$
81	392.3	310.9	$\cdots$	$\cdots$	-6.90	1.63	0.3	$\cdots$	$\cdots$	$\cdots$
82	463.0	313.7	$\cdots$	$\cdots$	-3.73	1.90	0.3	$\cdots$	$\cdots$	$\cdots$
83	$\cdots$	$\cdots$	487.0	639.1	-3.60	1.99	$\cdots$	0.9	$\cdots$	$\cdots$
84	655.8	314.3	407.4	267.1	4.88	2.96	0.7	5.6	0.06	3.8
85	641.3	314.9	$\cdots$	$\cdots$	4.23	2.85	0.2	$\cdots$	$\cdots$	$\cdots$
86	$\cdots$	$\cdots$	495.9	606.2	-2.89	1.72	$\cdots$	0.6	$\cdots$	$\cdots$
87	420.9	320.8	$\cdots$	$\cdots$	-5.57	1.35	0.2	$\cdots$	$\cdots$	$\cdots$
88	652.5	321.2	$\cdots$	$\cdots$	4.77	2.63	0.2	$\cdots$	$\cdots$	$\cdots$
89	645.0	321.8	427.9	282.1	4.44	2.56	0.2	0.7	$\cdots$	$\cdots$

TABLE 5. (continued)

No.	X PC	Y PC	X FOC	Y FOC	$\Delta\alpha('')$	$\Delta\delta('')$	f_λ 6060 Å	f_λ 2270 Å	$R('')$	R (pc)
(1)	(2)	(3)	(4)	(5)	(6)	(7)	(8)	(9)	(10)	(11)
90	630.9	321.9	$\cdots$	$\cdots$	3.81	2.48	0.6	$\cdots$	$\cdots$	$\cdots$
91	665.9	322.2	$\cdots$	$\cdots$	5.37	2.66	0.3	$\cdots$	$\cdots$	$\cdots$
92	465.9	323.7	$\cdots$	$\cdots$	-3.54	1.47	0.3	$\cdots$	$\cdots$	$\cdots$
93	417.9	326.7	$\cdots$	$\cdots$	-5.67	1.07	0.2	$\cdots$	$\cdots$	$\cdots$
94	633.5	326.7	$\cdots$	$\cdots$	3.95	2.28	0.4	$\cdots$	$\cdots$	$\cdots$
95	$\cdots$	$\cdots$	446.9	298.6	4.11	2.12	$\cdots$	0.4	$\cdots$	$\cdots$
96	443.1	327.8	530.0	677.4	-4.54	1.16	0.4	2.3	$\cdots$	$\cdots$
97	511.8	328.1	$\cdots$	$\cdots$	-1.47	1.54	0.3	$\cdots$	$\cdots$	$\cdots$
98	655.8	328.2	434.0	260.0	4.96	2.34	1.9	5.2	0.03	2.3
99	429.2	330.5	$\cdots$	$\cdots$	-5.14	0.96	0.3	$\cdots$	$\cdots$	$\cdots$
100	603.0	331.2	$\cdots$	$\cdots$	2.62	1.91	0.4	$\cdots$	$\cdots$	$\cdots$
101	642.7	332.2	$\cdots$	$\cdots$	4.39	2.09	0.3	$\cdots$	$\cdots$	$\cdots$
102	436.0	332.3	$\cdots$	$\cdots$	-4.83	0.92	0.2	$\cdots$	$\cdots$	$\cdots$
103	448.6	333.0	$\cdots$	$\cdots$	-4.27	0.96	0.2	$\cdots$	$\cdots$	$\cdots$
104	445.9	335.0	$\cdots$	$\cdots$	-4.37	0.86	0.4	$\cdots$	$\cdots$	$\cdots$
105	656.3	335.5	$\cdots$	$\cdots$	5.02	2.01	0.3	$\cdots$	$\cdots$	$\cdots$
106	647.6	337.0	456.0	271.6	4.64	1.90	1.1	1.8	$\cdots$	$\cdots$
107	475.0	337.7	$\cdots$	$\cdots$	-3.06	0.90	0.3	$\cdots$	$\cdots$	$\cdots$
108	447.9	338.4	$\cdots$	$\cdots$	-4.27	0.72	0.3	$\cdots$	$\cdots$	$\cdots$
109	438.9	339.0	$\cdots$	$\cdots$	-4.67	0.64	0.4	$\cdots$	$\cdots$	$\cdots$
110	669.0	339.7	$\cdots$	$\cdots$	5.61	1.90	0.5	$\cdots$	$\cdots$	$\cdots$
111	450.7	344.8	$\cdots$	$\cdots$	-4.11	0.44	0.3	$\cdots$	$\cdots$	$\cdots$
112	442.5	354.8	$\cdots$	$\cdots$	-4.42	-0.05	0.3	$\cdots$	$\cdots$	$\cdots$
113	637.9	355.2	$\cdots$	$\cdots$	4.31	1.03	0.4	$\cdots$	$\cdots$	$\cdots$
114	429.4	357.3	$\cdots$	$\cdots$	-4.99	-0.23	0.2	$\cdots$	$\cdots$	$\cdots$
115	406.0	358.9	$\cdots$	$\cdots$	-6.02	-0.43	0.2	$\cdots$	$\cdots$	$\cdots$
116	635.7	360.7	$\cdots$	$\cdots$	4.24	0.77	0.2	$\cdots$	$\cdots$	$\cdots$
117	449.8	361.9	$\cdots$	$\cdots$	-4.05	-0.32	0.2	$\cdots$	$\cdots$	$\cdots$
118	678.0	363.7	494.6	200.6	6.15	0.87	0.8	3.0	0.05	3.0
119	678.1	372.2	511.8	196.1	6.20	0.50	1.1	3.2	0.04	2.6
120	$\cdots$	$\cdots$	543.6	279.1	4.33	-0.08	$\cdots$	0.4	$\cdots$	$\cdots$
121	620.9	381.9	$\cdots$	$\cdots$	3.70	-0.25	0.3	$\cdots$	$\cdots$	$\cdots$
122	642.6	386.3	$\cdots$	$\cdots$	4.70	-0.33	0.4	$\cdots$	$\cdots$	$\cdots$
123	$\cdots$	$\cdots$	558.0	266.1	4.59	-0.44	$\cdots$	0.6	$\cdots$	$\cdots$
124	624.4	390.8	570.2	297.0	3.91	-0.63	0.3	1.1	$\cdots$	$\cdots$
125	635.2	394.9	575.4	268.6	4.41	-0.76	3.6	9.5	0.04	2.6
126	624.3	396.9	$\cdots$	$\cdots$	3.94	-0.91	0.3	$\cdots$	$\cdots$	$\cdots$
127	643.2	398.7	$\cdots$	$\cdots$	4.79	-0.88	0.8	$\cdots$	$\cdots$	$\cdots$
128	457.5	399.7	$\cdots$	$\cdots$	-3.50	-1.97	0.3	$\cdots$	$\cdots$	$\cdots$
129	636.6	400.6	$\cdots$	$\cdots$	4.50	-1.00	0.2	$\cdots$	$\cdots$	$\cdots$
130	645.7	400.6	$\cdots$	$\cdots$	4.91	-0.95	0.4	$\cdots$	$\cdots$	$\cdots$
131	630.1	402.4	$\cdots$	$\cdots$	4.23	-1.12	0.5	$\cdots$	$\cdots$	$\cdots$
132	591.2	404.3	$\cdots$	$\cdots$	2.50	-1.42	0.3	$\cdots$	$\cdots$	$\cdots$
133	328.8	407.3	$\cdots$	$\cdots$	-9.20	-3.03	0.1	$\cdots$	$\cdots$	$\cdots$
134	686.7	409.3	$\cdots$	$\cdots$	6.80	-1.11	0.5	$\cdots$	$\cdots$	$\cdots$

TABLE 5. (continued)

No.	X PC	Y PC	X FOC	Y FOC	$\Delta\alpha('')$	$\Delta\delta('')$	f_λ 6060 Å	f_λ 2270 Å	$R('')$	R (pc)
(1)	(2)	(3)	(4)	(5)	(6)	(7)	(8)	(9)	(10)	(11)
135	617.2	411.2	$\cdots$	$\cdots$	3.70	-1.58	0.2	$\cdots$	$\cdots$	$\cdots$
136	457.9	413.0	$\cdots$	$\cdots$	-3.40	-2.56	0.2	$\cdots$	$\cdots$	$\cdots$
137	567.7	415.2	644.5	390.6	1.51	-2.04	0.3	0.6	$\cdots$	$\cdots$
138	538.9	420.4	$\cdots$	$\cdots$	0.26	-2.43	0.4	$\cdots$	$\cdots$	$\cdots$
139	676.8	423.9	$\cdots$	$\cdots$	6.43	-1.82	0.3	$\cdots$	$\cdots$	$\cdots$
140	568.7	437.0	$\cdots$	$\cdots$	1.68	-3.01	0.3	$\cdots$	$\cdots$	$\cdots$
141	663.3	437.9	$\cdots$	$\cdots$	5.91	-2.52	0.2	$\cdots$	$\cdots$	$\cdots$
142	512.3	438.7	$\cdots$	$\cdots$	-0.83	-3.40	0.2	$\cdots$	$\cdots$	$\cdots$
143	611.3	444.1	$\cdots$	$\cdots$	3.62	-3.09	0.2	$\cdots$	$\cdots$	$\cdots$
144	456.9	467.8	$\cdots$	$\cdots$	-3.14	-5.01	0.3	$\cdots$	$\cdots$	$\cdots$
145	451.3	469.2	$\cdots$	$\cdots$	-3.38	-5.11	0.4	$\cdots$	$\cdots$	$\cdots$
146	467.6	469.9	$\cdots$	$\cdots$	-2.65	-5.04	0.4	$\cdots$	$\cdots$	$\cdots$
147	556.2	471.9	$\cdots$	$\cdots$	1.32	-4.64	0.6	$\cdots$	$\cdots$	$\cdots$
148	600.7	472.8	$\cdots$	$\cdots$	3.31	-4.43	0.1	$\cdots$	$\cdots$	$\cdots$
149	477.9	474.2	$\cdots$	$\cdots$	-2.16	-5.18	0.2	$\cdots$	$\cdots$	$\cdots$
150	463.8	476.9	$\cdots$	$\cdots$	-2.78	-5.38	0.2	$\cdots$	$\cdots$	$\cdots$
151	599.1	479.1	$\cdots$	$\cdots$	3.27	-4.72	0.9	$\cdots$	$\cdots$	$\cdots$
152	465.7	480.1	$\cdots$	$\cdots$	-2.68	-5.51	0.2	$\cdots$	$\cdots$	$\cdots$
153	484.9	491.8	$\cdots$	$\cdots$	-1.75	-5.93	0.1	$\cdots$	$\cdots$	$\cdots$
154	489.2	499.9	$\cdots$	$\cdots$	-1.52	-6.27	0.3	$\cdots$	$\cdots$	$\cdots$
155	434.6	502.3	$\cdots$	$\cdots$	-3.94	-6.68	0.2	$\cdots$	$\cdots$	$\cdots$
156	586.6	514.2	$\cdots$	$\cdots$	2.91	-6.36	0.2	$\cdots$	$\cdots$	$\cdots$
157	532.9	514.3	$\cdots$	$\cdots$	0.52	-6.66	0.2	$\cdots$	$\cdots$	$\cdots$

Notes to Table 5.

(1) – Source No. 0 denotes the coordinate origin, at the approximate geometrical center of the ring; (2)(3)(4)(5) – X and Y pixel coordinates on the PC chip of the WFPC2 and on the FOC; (6)(7) – Offset in arseconds from the origin (source No. 0), in the R.A. and Decl. directions; (8)(9) – f_λ(2270Å) and f_λ(6060Å) in units of 10^{-17} erg s^{-1} cm^{-2} Å^{-1}; (10) – σ of best-fit Gaussian width (see text), in arcseconds; (11) – As in (12), assuming distance in Table 1.

TABLE 6. Compact Sources – NGC 5248

No. (1)	X (2)	Y (3)	$\Delta\alpha('')$ (4)	$\Delta\delta('')$ (5)	$f_\lambda(2270\text{Å})$ (6)	$R('')$ (7)	R (pc) (8)
0	601.0	547.0	0.00	0.00	$\cdots$	$\cdots$	$\cdots$
1	275.0	843.6	-8.12	5.69	3.2	0.04	4.4
2	291.4	831.8	-7.78	5.39	28.1	≤ 0.03	≤ 3.7
3	466.9	833.9	-6.96	1.52	7.7	≤ 0.03	≤ 3.7
4	451.5	821.7	-6.77	1.92	2.1	$\cdots$	$\cdots$
5	462.0	803.9	-6.33	1.78	0.5	$\cdots$	$\cdots$
6	448.7	800.3	-6.31	2.09	2.4	$\cdots$	$\cdots$
7	392.4	735.1	-5.16	3.65	2.3	$\cdots$	$\cdots$
8	325.4	666.5	-3.99	5.46	4.3	≤ 0.03	≤ 3.7
9	290.6	651.0	-3.82	6.30	1.0	$\cdots$	$\cdots$
10	224.8	460.1	0.04	8.69	2.4	$\cdots$	$\cdots$
11	413.1	530.9	-0.58	4.20	1.7	$\cdots$	$\cdots$
12	418.0	521.2	-0.34	4.14	0.7	$\cdots$	$\cdots$
13	700.2	702.2	-2.92	-2.95	1.4	$\cdots$	$\cdots$
14	693.0	677.5	-2.41	-2.67	12.2	0.05	5.6
15	695.8	655.1	-1.90	-2.61	2.3	$\cdots$	$\cdots$
16	702.0	643.6	-1.62	-2.70	5.2	0.06	6.2
17	609.0	492.1	1.24	0.10	3.5	0.09	10.0
18	801.1	431.9	3.52	-3.82	6.6	0.05	5.0
19	714.6	404.4	3.69	-1.79	2.6	$\cdots$	$\cdots$
20	758.0	384.2	4.35	-2.64	1.4	$\cdots$	$\cdots$
21	804.6	330.8	5.75	-3.40	3.0	0.04	4.4
22	932.1	241.6	8.34	-5.75	0.8	$\cdots$	$\cdots$
23	901.0	246.2	8.09	-5.10	4.1	≤ 0.03	≤ 3.7
24	749.1	310.5	5.92	-2.08	2.6	$\cdots$	$\cdots$
25	719.0	334.0	5.26	-1.54	0.3	$\cdots$	$\cdots$
26	541.0	368.5	3.62	2.20	3.5	0.04	4.4
27	541.1	360.3	3.80	2.24	1.6	$\cdots$	$\cdots$
28	562.8	344.1	4.26	1.84	1.0	$\cdots$	$\cdots$
29	581.7	332.9	4.60	1.48	1.3	$\cdots$	$\cdots$
30	608.9	315.6	5.12	0.97	4.3	0.08	8.7
31	653.6	303.9	5.60	0.05	11.1	0.05	5.0
32	645.1	269.6	6.31	0.41	1.3	$\cdots$	$\cdots$
33	638.9	249.8	6.71	0.64	3.0	0.06	6.2
34	603.5	214.8	7.30	1.59	5.3	0.05	5.0
35	571.5	223.4	6.96	2.25	2.2	$\cdots$	$\cdots$
36	309.1	682.4	-4.42	5.74	1.6	$\cdots$	$\cdots$
37	350.4	635.7	-3.19	5.06	3.1	0.10	11.2
38	348.2	609.1	-2.61	5.24	3.0	0.10	11.2
39	219.5	443.8	0.38	8.88	1.9	$\cdots$	$\cdots$
40	336.9	414.9	1.59	6.45	1.3	$\cdots$	$\cdots$
41	709.1	675.4	-2.28	-3.01	0.4	$\cdots$	$\cdots$
42	700.3	650.6	-1.78	-2.69	5.4	0.10	11.2
43	777.8	432.5	3.39	-3.31	1.7	$\cdots$	$\cdots$
44	765.9	421.6	3.57	-3.00	0.5	$\cdots$	$\cdots$
45	772.6	426.9	3.49	-3.17	1.0	$\cdots$	$\cdots$
46	617.9	333.1	4.78	0.69	2.4	$\cdots$	$\cdots$

Notes to Table 6.

See Table 2 notes

TABLE 7. NGC 2997 – Cluster Luminosities and Colors

Source (1)	$\log L_\lambda(2270\,\text{Å})$ (2)	$\log L_\lambda(6060\,\text{Å})$ (3)	$\log\left(\dfrac{f_\lambda(6060\,\text{Å})}{f_\lambda(2270\,\text{Å})}\right)$ (4)	R (pc) (5)
5	35.65	34.88	-0.77	$\cdots$
9	35.48	34.78	-0.69	$\cdots$
12	35.24	35.02	-0.22	$\cdots$
18	35.70	34.86	-0.85	$\cdots$
38	35.89	35.07	-0.82	5.3
46	36.78	36.22	-0.56	≤ 2.3
58	35.95	35.51	-0.45	≤ 2.3
60	35.84	35.32	-0.52	≤ 2.3
63	35.46	34.79	-0.67	$\cdots$
64	36.21	35.59	-0.62	3.0
67	35.93	35.30	-0.64	2.6
69	36.08	35.57	-0.51	3.4
71	35.30	34.59	-0.71	$\cdots$
77	36.05	35.46	-0.59	2.6
84	36.10	35.19	-0.91	3.8
89	35.21	34.66	-0.55	$\cdots$
96	35.72	34.92	-0.81	$\cdots$
98	36.07	35.63	-0.44	≤ 2.3
106	35.60	35.41	-0.20	$\cdots$
118	35.84	35.24	-0.60	3.0
119	35.87	35.40	-0.47	2.6
124	35.41	34.76	-0.64	$\cdots$
125	36.34	35.92	-0.42	2.6
137	35.14	34.84	-0.30	$\cdots$

Notes to Table 7.

Sources from Table 5 detected in both bands; (2)(3) – L_λ in units of erg s^{-1} Å^{-1}, assuming distance in Table 1 and no extinction; (5) – See notes to Table 5.